Mechatronics 88 (2022) 102910

Contents lists available at ScienceDirect

Mechatronics

journal homepage: www.elsevier.com/locate/mechatronics

Optimal trajectory smoothing for direct energy deposition additive manufacturing processes☆

Emilio Perez [a], Robert Landers [b,*], Douglas Bristow [a]

[a] Department of Mechanical and Aerospace Engineering, Missouri University of Science and Technology, 400 West 13th Street, Rolla, MO 65409-0050, United States
[b] Department of Aerospace and Mechanical Engineering, University of Notre Dame, 152 Multidisciplinary Research Building, Notre Dame, IN 46556-0458, United States

ARTICLE INFO

Associate Editor: Prof Chris Manzie

Keywords:
Additive manufacturing
Trajectory planning

ABSTRACT

In free form additive manufacturing processes (e.g., metal blown powder, glass filament, ceramic paste extrusion), part quality depends on both the rate at which the part is built and where material is deposited. This creates a natural conflict between these two criteria at locations where the curvature of the programmed path is small, such as corners, because at these locations it is not possible to precisely follow the path without changing acceleration and, hence, varying the part build rate due to the variation in path velocity. In some additive manufacturing processes it is not possible to easily vary the material feed rate to maintain a constant part build rate when path velocity varies; thus, uneven material deposition occurs. In this work an optimal trajectory smoothing methodology is created that formulates the path following problem as an optimal dynamic system boundary value problem. The methodology naturally allows a trade-off between path following error and velocity error and is experimentally applied in a blown powder direct metal deposition additive manufacturing process. The results show that path and velocity errors increase as the corner angle decreases and the velocity entering the corner increases; however, they can be decreased by increasing the corner's leg length. Further, as the weight on velocity error increases, the velocity error, excess deposited material, and total print time decrease asymptotically while path error increases asymptotically.

1. Introduction

Additive Manufacturing (AM) has garnered much attention for its ability to repair or modify parts, open up the design space by fabricating parts with functionally graded materials and complex geometries, and build parts with substantially less waste compared to subtractive manufacturing processes. Additive manufacturing processes fuse filaments, powders, rods, or other stock material together, typically layer by layer, to build the desired part. The part morphology and its geometric quality are highly related to the relative velocity between the material being deposited and the substrate upon which the part is built, as well as the variations in that velocity, and to the placement of the material.

Parts in AM processes are first designed using a Computer-Aided Design software. The designed part is output as a Stereolithographic (STL) file which is interpreted by a slicer program. Slicer programs "slice" the STL file into layers, or planar cross sections of the STL, such that a programmed path is created in each layer. The programmed path is the motion the manufacturing machine must follow to build the given part and is created in a process called path planning. In layer-based AM, the toolpath consists of the programmed machine path for each layer joined by an incremental offset in the vertical direction to connect each layer. After generating the path, the path is output as instructions interpretable by the AM machine, usually in a text-based format called G-code.

Additive manufacturing path planning is concerned with generating the path geometry. Depending on the AM process, different path planning methods will affect part quality by affecting geometric accuracy, surface quality, and the number and size of voids present in the part. Different infill patterns have been shown to improve the build quality for specific processes [1–3]. Ding et al. investigated a path planning algorithm for wire-and-arc additive manufacturing which utilized the medial axis transformation [1,2]. Compared to contour-parallel, zig-zag, and raster path planning, medial axis transform path planning provided much better geometric accuracy and the elimination of voids when used with wire-and-arc AM. For fused deposition modelling processes, Jin et al. proposed a path planning algorithm based on direction-parallel paths which determined the optimal degree of inclination, and

☆ This paper was recommended for publication by Associate Editor Prof Chris Manzie.

* Corresponding author.
E-mail address: rlanders@nd.edu (R. Landers).

https://doi.org/10.1016/j.mechatronics.2022.102910
Received 5 April 2022; Received in revised form 30 July 2022; Accepted 12 October 2022
Available online 29 October 2022
0957-4158/© 2022 Elsevier Ltd. All rights reserved.

Nomenclature

A, $\bar{A}$	acceleration and normalized acceleration
A_0	estimated maximum acceleration
$A_{\max}$	maximum allowable acceleration
$CS_{Area,\text{abs int}}$	print cross-sectional area absolute integral
$CS_{AvgHeight}$	print cross-section average height
E, $\bar{E}$	contour error and normalized contour error
$E_{\text{abs int}}$	normalized contour error absolute integral
E_{int}	normalized contour error squared integral
$E_{\max}$	maximum normalized contour error
$\mathbf{e}_1$, $\mathbf{e}_2$	corner leg unit vectors
$\mathbf{e}_{1,i}$, $\mathbf{e}_{2,i}$	corner leg unit vectors extracted from straight-line motions
H	Hamiltonian
h	maximum perpendicular distance between optimal path and bisector
J	cost function
L	spatial normalization constant
$\mathbf{L}_i$	constant velocity linear path
l	corner leg length
l_i	corner leg lengths extracted from straight-line motions
$l_{L,i}$	constant velocity linear path length
$\mathbf{P}_i$	corner points extracted from straight-line motions
$\mathbf{p}_0$, $\mathbf{p}_1$, $\mathbf{p}_2$	start, corner, and end point Cartesian coordinates
$\mathbf{p}_{0,i}$, $\mathbf{p}_{2,i}$	start and end point Cartesian coordinates extracted from straight-line motions
q	velocity error optimization weight
$\mathbf{R}_{-\beta}$, $\mathbf{R}_{-\beta,1}$, $\mathbf{R}_{-\beta,2}$	path rotation matrix, first/second rows of path rotation matrix
r	acceleration optimization weight
$\mathbf{r}$, $\bar{\mathbf{r}}$	optimal corner path and normalized corner path
$\mathbf{r}_1$, $\mathbf{r}_2$, $\bar{\mathbf{r}}_1$, $\bar{\mathbf{r}}_2$	first and second half of optimal path, and normalized values
s	contour error optimization weight
T	time normalization constant
t, $\bar{t}$	time and normalized time
t_0, t_1, t_2, $\bar{t}_0$, $\bar{t}_1$, $\bar{t}_2$	start point, mid-point, and end point times, and normalized values
$\mathbf{u}$	control input vector
V_0	nominal velocity
V_{err}, $\bar{V}_{err}$	velocity error and normalized velocity error
$V_{err,\text{abs int}}$	absolute integral of normalized velocity error
$V_{err,\text{int}}$	squared integral of normalized velocity error
$V_{err,\max}$	maximum of normalized velocity error
$\mathbf{Z}$	state variable vector
β	angle of corner path bisector
$\boldsymbol{\lambda}$	system co-state vector
θ	absolute angle of corner
θ_1, θ_2	first and second corner leg angle
$\theta_{1,i}$, $\theta_{2,i}$	first and second corner leg angle extracted from straight-line motions

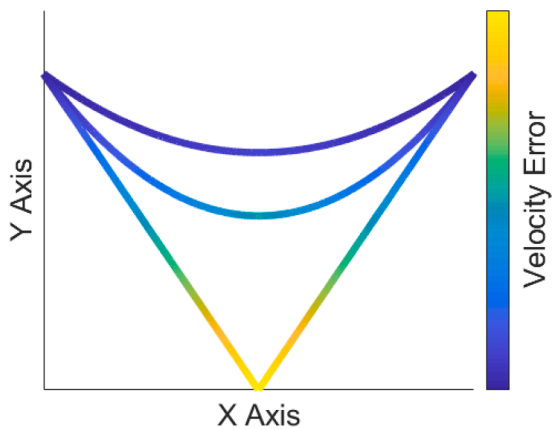

Fig. 1. Velocity errors for various paths used to fabricate a sharp corner.

generated, grouped, and linked sub-paths [3]. In the case of multi-axis printing, curved layers instead of flat layers may be used to improve printing quality [4].

Trajectory planning is often implemented after path planning to fit velocity profiles to the path, often using trapezoidal velocity, s-curves, or another standard kinematic profile. Alternatively, optimization techniques may be used for trajectory planning to improve the manufacturing process. In AM processes, the spatial distribution of material deposited depends on the material feed rate and path velocity. This spatial distribution is highly correlated with part geometric quality. Thus, optimizing the path by synchronizing the material feed rate and print velocity is usually done to ensure even material deposition. In most cases, in a process called path smoothing, curvature is also added to the path to minimize the velocity variations at the expense of position error. The tradeoff between velocity variations and position error is illustrated in Fig. 1. As the programmed path is closer to the reference path, in this case the corner, the contour errors decrease while the velocity errors increase.

Ertay et al. presented a methodology to plan and synchronize the path's speed and the material feed rate for extrusion-based AM processes [5]. This methodology uses a thermal model to determine the extrusion rate of a plastic filament for the fused deposition modelling process. After fitting a Non-Uniform Rational B-Spline (NURBS) curve to the path, the path's parametric feed rate was optimized so that the material feed rate and path speed are synchronized. Han and Jafari designed a discrete time control system to regulate the material feed rate and path speed so that their ratio is kept nearly constant in real time [6]. Giberti et al. proposed a path planning algorithm which maintains a near-constant path speed by smoothing corners using Bezier curves [7]. Comminal et al. proposed smoothing corners with a blended acceleration trajectory where the user can modify the amount of corner smoothing with a blending factor variable [8].

Trajectory optimization is also done for subtractive manufacturing processes; however, the toolpath speed can vary more freely because slowing down or stopping typically does not affect the total amount of material removed and part quality. Generally, the goal of trajectory optimization for subtractive manufacturing processes is to minimize the time to fabricate the part while accounting for machine limits, e.g., maximum acceleration and jerk. Typically, subtractive manufacturing trajectory optimization is conducted by predefining the path's position geometry and optimizing the parametric feed rate, which is an intermediate variable describing the path's temporal space and affects the path's time derivatives. By predefining the part geometry, it is possible to exploit geometric path properties to simplify the trajectory optimization procedure. For example, Ernesto and Farouki presented a corner smoothing method which prespecified the path as a rational Bezier curve to easily account for acceleration and position constraints [9]. Ernesto and Farouki optimized the feed rate profile to minimize the time needed to traverse the path. Similar approaches are employed in [10] and [11]. Sometimes, the geometry and feed rate profile are optimized simultaneously by using optimal control methods [12–14]. Such is the case in the work of Duan and Okwudire, where a corner smoothing method which determines the time-optimal free-form curve was presented [14].

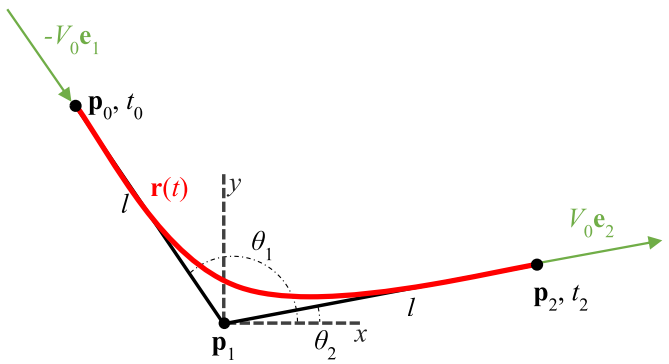

Fig. 2. Corner region diagram.

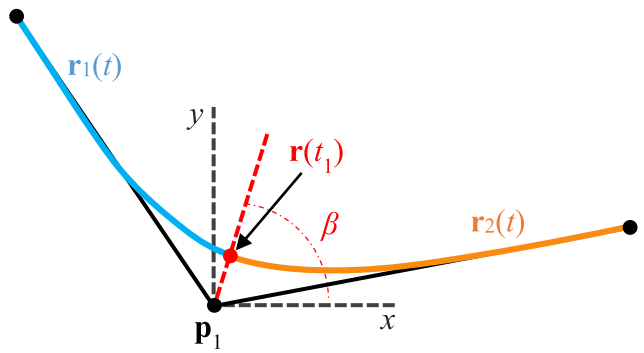

Fig. 3. Corner region diagram showing r(t_1) and bisecting line.

Duan and Okwudire [14] used an optimal control method to recast the path planning problem as a two-point boundary value problem and determined the free-form curve, which was then parameterized as a NURBS curve using a least-squares algorithm. By using an optimal control method to define the path, Duan and Okwudire [14] removed the necessity of prespecifying any curve geometry, guaranteeing the best free-form curve. While [9–14] are optimal trajectory planning methodologies that regulate contour errors and machining time given acceleration constraints, they do not directly regulate velocity errors.

In free form AM processes (e.g., metal blown powder, glass filament and ceramic paste extrusion), the part quality depends on both the rate at which material is deposited and where the material is deposited. This creates a natural conflict between these two criteria at sections where the curvature of the programmed path is small, such as corners, because it is not possible to precisely follow the path without changing acceleration and, hence, varying the material deposition rate. Uneven material deposition is observed when a change in path velocity occurs and a constant material feed rate is used. Wherever it is possible, synchronizing the material feed rate and path velocity, along with minimizing their variations, should be done to maintain a uniform material deposition rate. In some cases, it is not always possible to do both, such as in Direct Metal Deposition (DMD) processes where there are large time delays when changing the material feed rate. In this paper we will consider the cases where material feed rate and path velocity cannot be synchronized.

In this article, a corner trajectory smoothing methodology that provides a systematic trade-off between path following errors and velocity errors is presented. Similar to [14], an optimal control method is used to recast the trajectory planning problem into a two-point boundary value problem to determine the optimal path. Instead of only including the final time of the path in the cost function, as was done in [14], the velocity error, contour error, and acceleration are included in the cost function due to their importance in AM processes. Section 2 details the mathematical definition and normalization of the optimal corner path and concludes with an analysis and discussion of optimal corner paths. In contrast to [14], no velocity error or contour error constraints are placed on the path, providing additional freedom for path design. Section 3 consists of an application of the methodology to the DMD printing process. Four different reference paths were printed on a DMD machine for a five-pointed star. Three of the paths used the methodology with different parameters corresponding to 25%, 50% and 75% maximum velocity errors. The last path followed the reference path exactly using trapezoidal velocity profiles with full-stops at each corner. Section 4 contains the summary and conclusions of the paper. Lastly, an appendix describing an iterative solver used in the optimization routine is given.

2. Corner smoothing methodology

2.1. Optimal path definition

Consider a region around a part corner, as shown in Fig. 2. A coordinate system is set such that $\mathbf{p}_1 = [0\ 0]^T$, where $\mathbf{p}_1$ is the corner point. The end points of the corner region are $\mathbf{p}_1 = \mathbf{p}_0 + l\mathbf{e}_1$ and $\mathbf{p}_2 = \mathbf{p}_1 + l\mathbf{e}_2$, where the exact path is from $\mathbf{p}_0$ to $\mathbf{p}_1$ to $\mathbf{p}_2$ and l is the leg length. The unit vectors $\mathbf{e}_1 = [\cos(\theta_1)\ \sin(\theta_1)]^T$ and $\mathbf{e}_2 = [\cos(\theta_2)\ \sin(\theta_2)]^T$ describe the direction information of the two legs, where θ_1 and θ_2 are defined in Fig. 2.

The optimal path is denoted,

$$\mathbf{r}(t) = [x(t) \quad y(t)]^T, \quad t \in [t_0, t_2], \tag{1}$$

where t_0 and t_2 are the times when the motion system is at $\mathbf{p}_0$ and $\mathbf{p}_2$, respectively. The position and velocity of the path at the end points, respectively, are,

$$\mathbf{r}(t_0) = \mathbf{p}_0, \quad \mathbf{r}(t_2) = \mathbf{p}_2, \tag{2}$$

$$\dot{\mathbf{r}}(t_0) = -V_0\mathbf{e}_1, \quad \dot{\mathbf{r}}(t_2) = V_0\mathbf{e}_2, \tag{3}$$

where V_0 is the desired nominal velocity.

Only the first half of the path is optimized since the path is symmetric about the corner's bisecting line. Fig. 3 shows the path split into two halves, denoted $\mathbf{r}_1(t)$ and $\mathbf{r}_2(t)$. The optimal path is rewritten as,

$$\mathbf{r}(t) = \begin{cases} \mathbf{r}_1(t) = [x_1(t) \quad y_1(t)]^T & t \in [t_0, t_1] \\ \mathbf{r}_2(t) = [x_2(t) \quad y_2(t)]^T & t \in [t_1, t_2] \end{cases}, \tag{4}$$

where t_1 is the time when the motion system is at $\mathbf{p}_1$. The angle of the bisector with respect to the x-axis is,

$$\beta = \frac{\theta_1 + \theta_2}{2}. \tag{5}$$

The path is rotated by -β to align the corner's bisecting line with the x-axis. This rotation is defined by,

$$\mathbf{R}_{-\beta} = \begin{bmatrix} \cos(-\beta) & -\sin(-\beta) \\ \sin(-\beta) & \cos(-\beta) \end{bmatrix} = \begin{bmatrix} \mathbf{R}_{-\beta,1} \\ \mathbf{R}_{-\beta,2} \end{bmatrix}, \tag{6}$$

with $\mathbf{R}_{-\beta,1}$ and $\mathbf{R}_{-\beta,2}$ defined as the first and second rows, respectively, of $\mathbf{R}_{-\beta}$. When the path undergoes this rotation, the following holds true for the corner position,

$$\mathbf{R}_{-\beta}\mathbf{r}(t_1) = \begin{bmatrix} x_\beta \\ 0 \end{bmatrix}, \tag{7}$$

where the value of x_β is the distance between $\mathbf{p}_1$ and $\mathbf{r}(t_1)$. The first continuity equation is given in the second row of (7),

$$\mathbf{R}_{-\beta,2}\mathbf{r}(t_1) = 0. \tag{8}$$

The velocity at the corner position is assumed to be perpendicular to the bisecting line; therefore, performing the same rotation on $\dot{\mathbf{r}}(t_1)$,

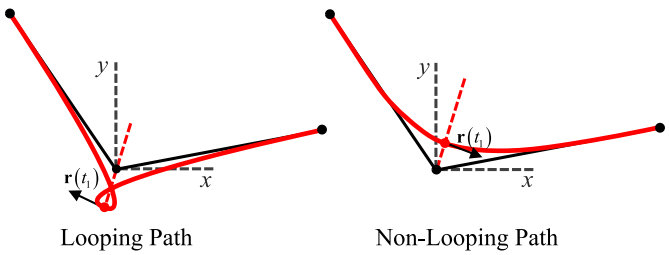

Fig. 4. Example of looping (left) and non-looping (right) paths.

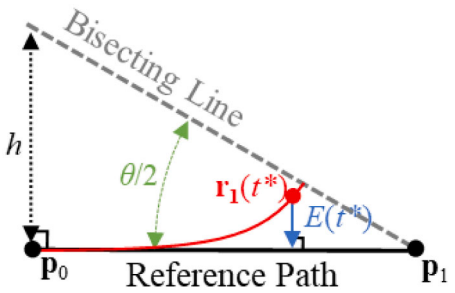

Fig. 5. Half corner region showing variables h, $\theta/2$, and E.

$$\mathbf{R}_{-\beta}\dot{\mathbf{r}}(t_1) = \begin{bmatrix} 0 \\ v_{y,\beta} \end{bmatrix}, \tag{9}$$

where $v_{y,\beta}$ is the magnitude of $\dot{\mathbf{r}}(t_1)$. The second continuity equation is given in the first row of

(9),

$$\mathbf{R}_{-\beta,1}\dot{\mathbf{r}}(t_1) = 0. \tag{10}$$

Focusing on the bottom half of the rotation, there are two cases depending on the sign of $v_{y,\beta}$: looping paths for $v_{y,\beta} > 0$ and non-looping paths for $v_{y,\beta} < 0$, which are illustrated in Fig. 4. Looping paths are not desirable for additive manufacturing applications since they will result in excessive material deposition at the corner.

The last condition for continuity at the corner position is found by analyzing the acceleration vector at that time,

$$\mathbf{R}_{-\beta,2}\ddot{\mathbf{r}}(t_1) = 0. \tag{11}$$

This condition constrains the direction of the acceleration to be in the direction of the bisecting line.

The contour error, shown in Fig. 5, is,

$$E(t) = |[\sin(-\theta_1) \quad \cos(-\theta_1)]\mathbf{r}_1(t)|. \tag{12}$$

The normalized velocity error is,

$$\overline{V}_{err}(t) = \frac{\left|\sqrt{\dot{\mathbf{r}}_1(t)^T\dot{\mathbf{r}}_1(t)} - V_0\right|}{V_0}. \tag{13}$$

where V_0 is the desired velocity along the path. The normalized acceleration is,

$$\overline{A}(t) = \frac{\sqrt{\ddot{\mathbf{r}}_1(t)^T\ddot{\mathbf{r}}_1(t)}}{A_{\max}}, \tag{14}$$

where $A_{\max}$ is the maximum acceleration of the motion system's individual axes. The contour error is normalized by the maximum perpendicular distance from the optimal path to its bisector as shown in Fig. 5,

$$\overline{E}(t) = \frac{E(t)}{h} \tag{15}$$

where

$$h = l\tan\left(\frac{\theta}{2}\right), \tag{16}$$

and

$$\theta = |\theta_1 - \theta_2|. \tag{17}$$

This definition of h is selected as it will naturally increase the normalized contour error for sharp corners that, in turn, will naturally increase its importance when trading off normalized contour and velocity errors.

The optimal path is found by minimizing the cost function,

$$J = \int_{t_0}^{t_1} \left(q(\overline{V}_{err}(t))^2 + \rho(\overline{A}(t))^2 + s(\overline{E}(t))^2\right)dt \tag{18}$$

subject to the constraints in (2), (3), (8), (10), and (11) where q, ρ, and s are the weights on the normalized velocity error, acceleration, and contour error, respectively. Acceleration is included in the cost function as it is the input to the path dynamic system (described below) and has a limited magnitude; therefore, it must be included as part of the trade-off between the errors, which is accomplished by modifying the weights. However, the acceleration should also be maximized within the axis acceleration limits so that there is no performance loss in terms of the path velocity and contour errors. The value of ρ is chosen such that,

$$\max\left(\max_t(\ddot{x}(t)), \max_t(\ddot{y}(t))\right) = A_{\max}. \tag{19}$$

An iterative routine, detailed in the Appendix, was used to compute the value of ρ for each solution.

To construct the other half of the path, denoted $\mathbf{r}_2(t)$, we note that the solution is symmetric about the bisecting line in Fig. 3. Given that the second half of the path is defined on the time interval $[t_1,t_2]$, the equations for $\mathbf{r}_2(t)$ and its first two derivatives, respectively, are,

$$\begin{aligned} \mathbf{r}_2(t+t_1) &= \mathbf{R}_{-\beta}^{-1}\begin{bmatrix} 1 & 0 \\ 0 & -1 \end{bmatrix}\mathbf{R}_{-\beta}\mathbf{r}_1(t_1 - t), \\ \dot{\mathbf{r}}_2(t+t_1) &= \mathbf{R}_{-\beta}^{-1}\begin{bmatrix} -1 & 0 \\ 0 & 1 \end{bmatrix}\mathbf{R}_{-\beta}\dot{\mathbf{r}}_1(t_1 - t), \\ \ddot{\mathbf{r}}_2(t+t_1) &= \mathbf{R}_{-\beta}^{-1}\begin{bmatrix} 1 & 0 \\ 0 & -1 \end{bmatrix}\mathbf{R}_{-\beta}\ddot{\mathbf{r}}_1(t_1 - t). \end{aligned} \tag{20}$$

The final time to complete the path is,

$$t_2 = 2t_1. \tag{21}$$

2.2. Path normalization and boundary value problem

The path and time are normalized, respectively, by,

$$\overline{\mathbf{r}}(\overline{t}) = \frac{\mathbf{r}(t)}{L}, \tag{22}$$

and

$$\overline{t} = \frac{t}{T}, \tag{23}$$

where L and T are in the units of the path $\mathbf{r}(t)$ and time t, respectively. Differentiating t with respect to $\overline{t}$,

$$\frac{dt}{d\overline{t}} = T. \tag{24}$$

Using (22) and (24), the path's normalized velocity and acceleration, respectively, are,

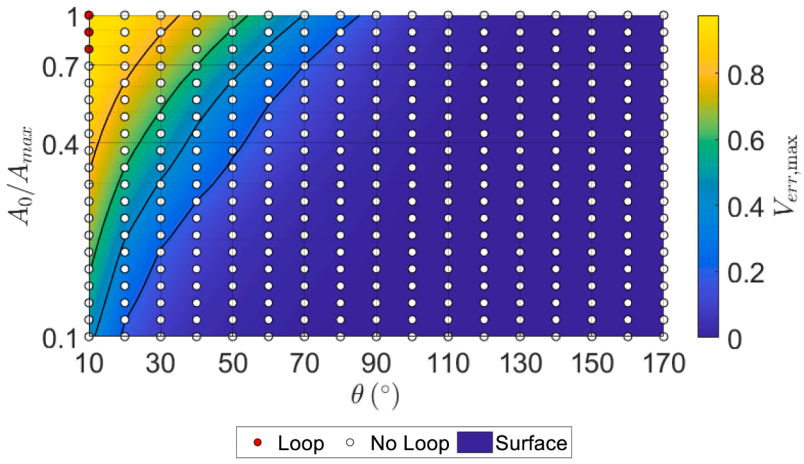

Fig. 6. $V_{err,\max}$ surface for $q/s = 1$ and $\beta = 0°$.

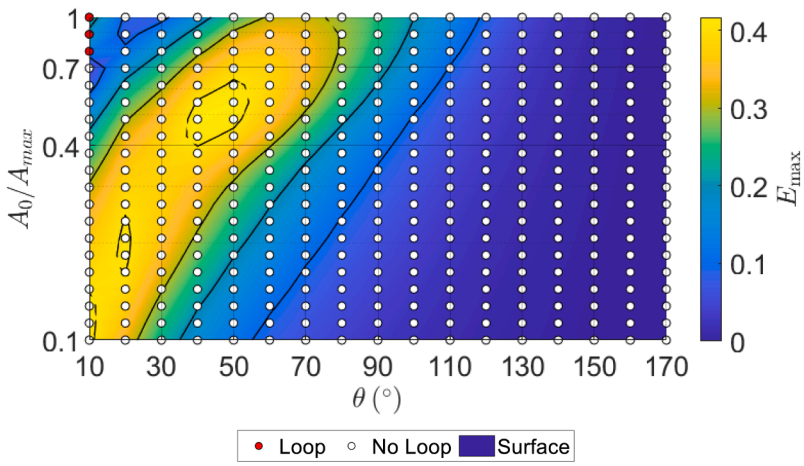

Fig. 7. $E_{\max}$ surface for $q/s = 1$ and $\beta = 0°$.

$$\bar{\mathbf{r}}'(\bar{t}) = \frac{\dot{\mathbf{r}}(t)}{L}\frac{dt}{d\bar{t}} = \frac{\dot{\mathbf{r}}(t)}{L/T},$$
$$\bar{\mathbf{r}}''(\bar{t}) = \frac{\ddot{\mathbf{r}}(t)}{L/T}\frac{dt}{d\bar{t}} = \frac{\ddot{\mathbf{r}}(t)}{L/T^2}. \tag{25}$$

Note that the operators $(\cdot)'$ and $(\cdot)''$ denote the first and second derivatives, respectively, of $\bar{\mathbf{r}}(\bar{t})$ with respect to $\bar{t}$. To normalize the velocity to V_0 and the acceleration to $A_{\max}$, values of $L/T = V_0$ and $L/T^2 = A_{\max}$ were chosen. While a variety of normalizations could be utilized, the selected normalizations have physical meaning for this problem as the normalized velocity is a fraction of the desired velocity along the path and the normalized acceleration is a fraction of the motion system's maximum acceleration. Using these values in (22), (23), and (25),

$$\bar{\mathbf{r}}(\bar{t}) = \frac{\mathbf{r}(t)}{V_0{}^2/A_{\max}}, \quad \bar{t} = \frac{t}{V_0/A_{\max}},$$
$$\bar{\mathbf{r}}'(\bar{t}) = \frac{\dot{\mathbf{r}}(t)}{V_0}, \quad \bar{\mathbf{r}}''(\bar{t}) = \frac{\ddot{\mathbf{r}}(t)}{A_{\max}}. \tag{26}$$

Next, the normalized contour error, velocity error, and acceleration, respectively, are rewritten in terms of the normalized path,

$$\bar{E}(t) = \frac{|[\sin(-\theta_1) \quad \cos(-\theta_1)]\bar{\mathbf{r}}_1(\bar{t})|}{\frac{A_{\max}}{A_0}\tan\left(\frac{\theta}{2}\right)},$$
$$\bar{V}_{err}(t) = \left|\sqrt{\bar{\mathbf{r}}'_1(\bar{t})^T\bar{\mathbf{r}}'_1(\bar{t})} - 1\right|,$$
$$\bar{A}(t) = \sqrt{\bar{\mathbf{r}}''_1(\bar{t})^T\bar{\mathbf{r}}''_1(\bar{t})}, \tag{27}$$

where

$$A_0 = \frac{V_0^2}{l}. \tag{28}$$

Based on (18) and (27), $\bar{\mathbf{r}}_1(\bar{t})$ only depends on $A_0/A_{\max}$, q/s, θ, and β when ρ is constant. The effect of ρ on the path was ignored since it was chosen such that (19) is true. Therefore, the normalization laid out in (26) halves the number of variables needed to analyze the path. Note the ratio $A_0/A_{\max}$ represents the fraction of maximum acceleration used during cornering.

Viewing the optimal path as a dynamical system transforms the optimization problem to a two-point boundary value problem. The state variables and control inputs, respectively, are defined as,

$$\mathbf{z} = \begin{bmatrix} z_1 \\ z_2 \\ z_3 \\ z_4 \end{bmatrix} = \begin{bmatrix} \bar{x}_1 \\ \bar{x}'_1 \\ \bar{y}_1 \\ \bar{y}'_1 \end{bmatrix} = u\begin{bmatrix} u_1 \\ u_2 \end{bmatrix} = \begin{bmatrix} \bar{x}''_1 \\ \bar{y}''_1 \end{bmatrix} \tag{29}$$

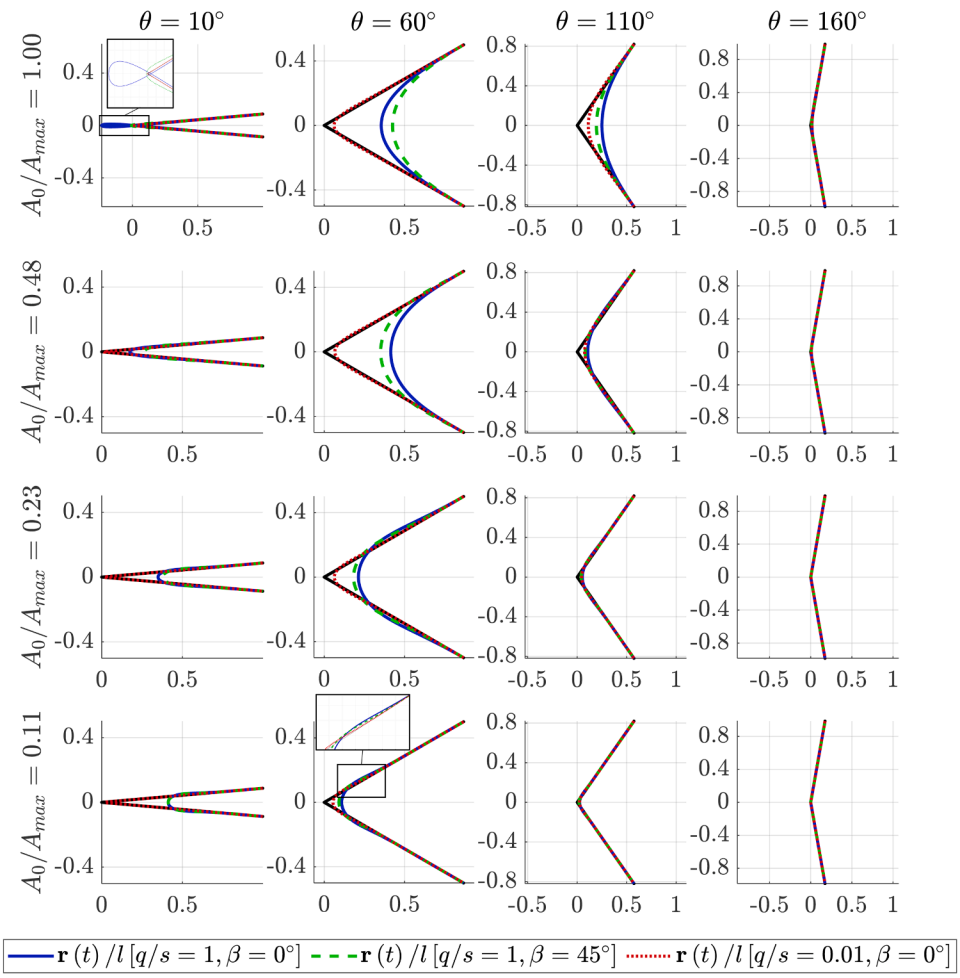

Fig. 8. Normalized path geometries for various combinations of q/s and β. Path with $\beta = 45°$ has been rotated $-45°$ for direct comparison with paths with $\beta = 0°$.

These definitions lead to the state-space description,

$$\mathbf{z}' = \begin{bmatrix} 0 & 1 & 0 & 0 \\ 0 & 0 & 0 & 0 \\ 0 & 0 & 0 & 1 \\ 0 & 0 & 0 & 0 \end{bmatrix} \mathbf{z} + \begin{bmatrix} 0 & 0 \\ 1 & 0 \\ 0 & 0 \\ 0 & 1 \end{bmatrix} \mathbf{u}. \tag{30}$$

The cost function in terms of these states is,

$$J = \frac{V_0}{A_{\max}} \int_{\bar{t}_0}^{\bar{t}_1} \left(q\left(\sqrt{\mathbf{z}^T Q \mathbf{z}} - 1\right)^2 + \rho\left(\mathbf{u}^T \mathbf{u}\right) + s\left(\frac{A_0}{A_{\max}} R_E \begin{bmatrix} 1 & 0 & 0 & 0 \\ 0 & 0 & 1 & 0 \end{bmatrix} \mathbf{z}\right)^2 \right) d\bar{t} \tag{31}$$

where

$$Q = \begin{bmatrix} 0 & 0 & 0 & 0 \\ 0 & 1 & 0 & 0 \\ 0 & 0 & 0 & 0 \\ 0 & 0 & 0 & 1 \end{bmatrix}, \quad R_E = \frac{\left[\sin(-\theta_1) \quad \cos(-\theta_1)\right]}{\tan\left(\frac{\theta}{2}\right)}. \tag{32}$$

The Hamiltonian for this optimal control problem is,

$$\begin{aligned} H(\mathbf{z}, \mathbf{u}, \lambda) &= q\left(\sqrt{\mathbf{z}^T Q \mathbf{z}} - 1\right)^2 + \rho \mathbf{u}^T \mathbf{u} + s\left(\frac{A_0}{A_{\max}} R_E \begin{bmatrix} 1 & 0 & 0 & 0 \\ 0 & 0 & 1 & 0 \end{bmatrix} \mathbf{z}\right)^2 \\ &\quad + \lambda^T \mathbf{z}' \\ &= q\left(\sqrt{{z_2}^2 + {z_4}^2} - 1\right)^2 + \rho\left({u_1}^2 + {u_2}^2\right) \\ &\quad + \cdots \frac{s}{\left(\frac{A_{\max}}{A_0} \tan\left(\frac{\theta}{2}\right)\right)^2} \left(\sin(-\theta_1) z_1 + \cos(-\theta_1) z_3\right)^2 + \lambda_1 z_2 + \lambda_2 u_1 \\ &\quad + \lambda_3 z_4 + \lambda_4 u_2 \end{aligned} \tag{33}$$

where $\boldsymbol{\lambda} = [\lambda_1\ \lambda_2\ \lambda_3\ \lambda_4]^T$ is the system co-state vector. Setting $\partial H/\partial \mathbf{u} = 0$, the optimal control signals are,

$$\mathbf{u} = -\begin{bmatrix} \frac{\lambda_2}{2\rho} & \frac{\lambda_4}{2\rho} \end{bmatrix}. \tag{34}$$

Setting $\partial H/\partial \mathbf{z} = -(\boldsymbol{\lambda}')^T$,

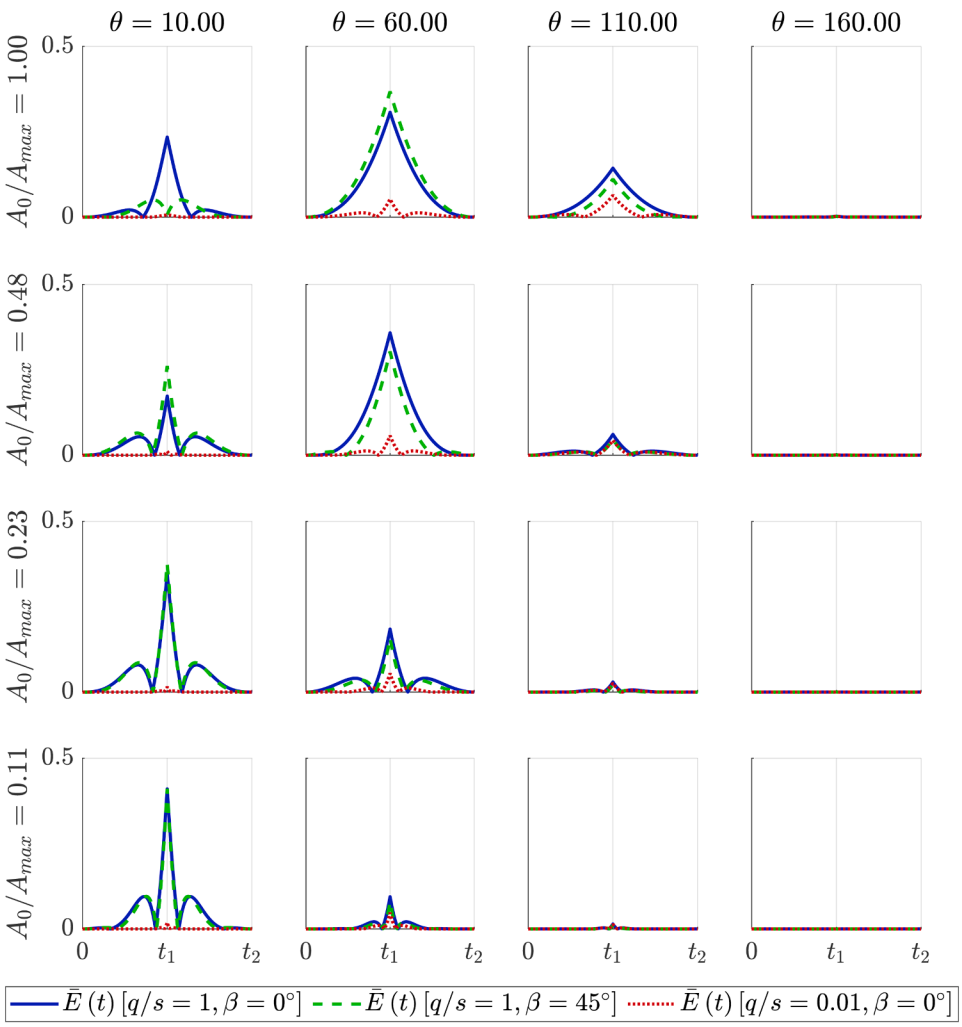

Fig. 9. Normalized contour error profiles for various combinations of q/s and β.

$$\lambda' = -\begin{bmatrix} \dfrac{2s\sin(-\theta_1)}{\left(\dfrac{A_{\max}}{A_0}\tan\left(\dfrac{\theta}{2}\right)\right)^2}(\sin(-\theta_1)z_1 + \cos(-\theta_1)z_3) \\ 2qz_2\left(1 - \dfrac{1}{\sqrt{{z_2}^2 + {z_4}^2}}\right) + \lambda_1 \\ \dfrac{2s\cos(-\theta_1)}{\left(\dfrac{A_{\max}}{A_0}\tan\left(\dfrac{\theta}{2}\right)\right)^2}(\sin(-\theta_1)z_1 + \cos(-\theta_1)z_3) \\ 2qz_4\left(1 - \dfrac{1}{\sqrt{{z_2}^2 + {z_4}^2}}\right) + \lambda_3 \end{bmatrix}. \tag{35}$$

Combining the system state and costate dynamic equations from (29) and (35), respectively, results in a system that is simulated using a boundary value problem solver. To implement this system, a total of nine boundary values are needed: one for each differential equation and one for the unknown final time t_1. The boundary conditions at $\bar{t}_0$ from (2) and (3) are,

$$\begin{bmatrix} z_1(\bar{t}_0) \\ z_2(\bar{t}_0) \\ z_3(\bar{t}_0) \\ z_4(\bar{t}_0) \end{bmatrix} = \begin{bmatrix} \dfrac{A_{\max}}{A_0}\cos\theta_1 \\ -\cos\theta_1 \\ \dfrac{A_{\max}}{A_0}\sin\theta_1 \\ -\sin\theta_1 \end{bmatrix}. \tag{36}$$

One boundary conditions at $\bar{t}_1$ is found by rewriting the condition in (11) using (34),

$$-\sin(-\beta)\lambda_2(\bar{t}_1) + \cos(-\beta)\lambda_4(\bar{t}_1) = 0. \tag{37}$$

Another boundary condition at $\bar{t}_1$, which has no physical meaning and was found numerically via repeated simulations, is,

$$\cos(-\beta)\lambda_1(\bar{t}_1) - \sin(-\beta)\lambda_3(\bar{t}_1) = 0. \tag{38}$$

The boundary conditions at $\bar{t}_1$ described in (8) and (10) are rewritten in terms of the elements of $\mathbf{z}$,

$$\begin{bmatrix} \sin(-\beta)z_1(\bar{t}_1) + \cos(-\beta)z_3(\bar{t}_1) \\ \cos(-\beta)z_2(\bar{t}_1) - \sin(-\beta)z_4(\bar{t}_1) \end{bmatrix} = \begin{bmatrix} 0 \\ 0 \end{bmatrix}. \tag{39}$$

The optimal path is found by numerically simulating the system with the boundary conditions at $\bar{t}_0$ described in (36), the boundary conditions at $\bar{t}_1$ described in (37)–(39), and with $\bar{t}_1$ free.

To account for the free final time, a change of variable $\tau = \bar{t}/\bar{t}_1$ is used to normalize the optimization interval to [0, 1]. The system is simulated by including $\bar{t}_1$ as an unknown parameter with dynamics described by,

$$\dot{\bar{t}}_1 = 0. \tag{40}$$

The final condition needed at $\bar{t}_1$ is derived from,

$$H(\mathbf{z}(\bar{t}_1), \mathbf{u}(\bar{t}_1), \lambda(\bar{t}_1)) = 0. \tag{41}$$

The MATLAB boundary value problem solver "*bvp4c*" was used to

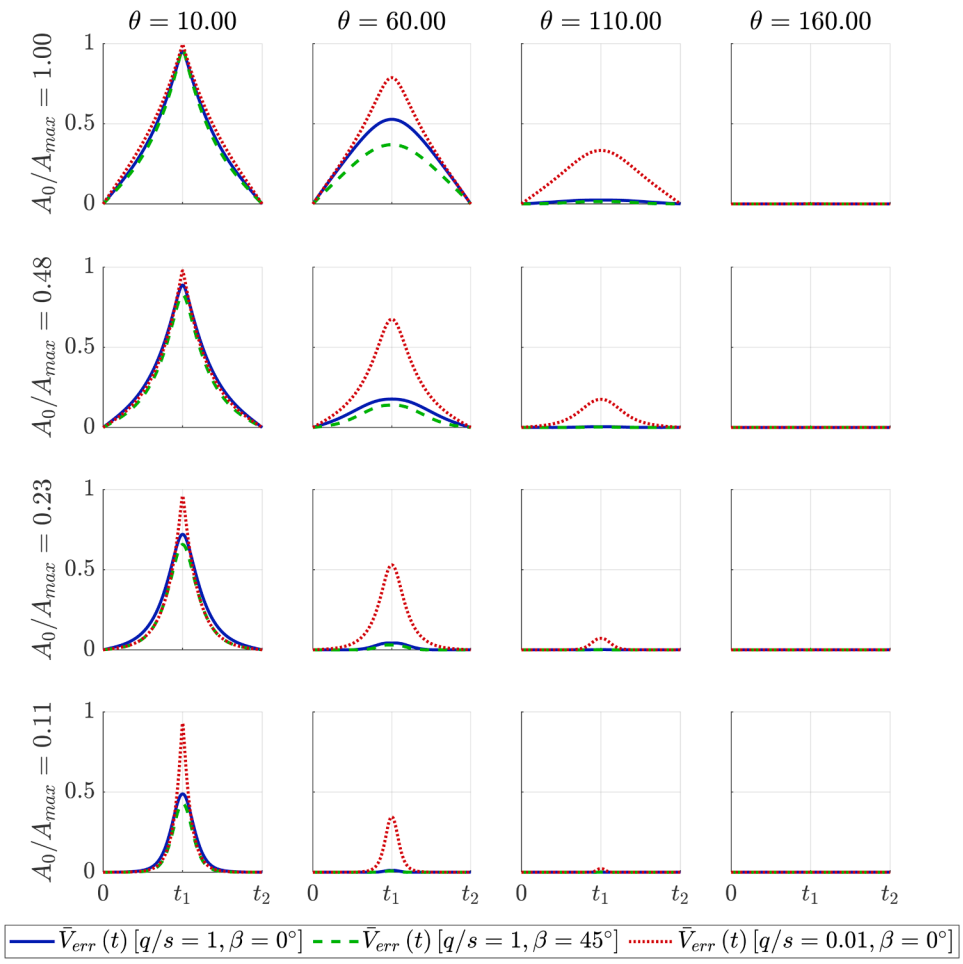

Fig. 10. Normalized velocity error profiles for various combinations of q/s and β.

numerically simulate the system. The value of ρ is chosen such that (19) is true to ensure the maximum axis acceleration is met and there is no velocity error and contour error performance loss. To determine ρ, an iterative routine was created and is detailed in the Appendix. Note that one must adjust the values of q and s in (31) to achieve specified levels of contour and velocity errors and to explore the space of possible errors. Alternatively, one could recast the problem as a constrained optimization problem where the level of contour (velocity) error is specified, and the velocity (contour) error is optimized. Adjusting q and s could be automated by selecting a value of q/s and decreasing this value until the required level of contour error is achieved. This process would be repeated for several values of q/s.

2.3. Analysis and discussion

To analyze the optimal path generation methodology proposed in this paper, maximum and time-integrated errors are examined. The maximum velocity and contour errors, respectively, are,

$$V_{err,\max} = \max_t(\overline{V}_{err}(t)), \tag{42}$$

$$E_{\max} = \max_t(\overline{E}(t)). \tag{43}$$

The squared integral velocity and squared integral contour errors, respectively, are,

$$V_{err,\text{int}} = 2\int_{t_0}^{t_1} (\overline{V}_{err}(t))^2 dt, \tag{44}$$

$$E_{\text{int}} = 2\int_{t_0}^{t_1} (\overline{E}(t))^2 dt. \tag{45}$$

Keeping q/s and β constant, the path errors as a function of $A_0/A_{\max}$ and θ were calculated using (42)–(45). Letting $q/s \in \{0.01, 1\}$, $\beta \in \{0°, 45°\}$, $A_0/A_{\max} \in [0.01, 1]$ with 20 logarithmically spaced points, and $\theta \in [10°, 170°]$ with 17 linearly spaced points, path error surfaces were created. The value of $A_0/A_{\max}$ was modified by setting $A_{\max} = 1$ mm/s^2, $V_0 = 1$ mm/s, and increasing l from 1 to 10 mm. Figs. 6 and 7 show the $V_{err,\max}$ and $E_{\max}$ surfaces, respectively, when $q/s = 1$ and $\beta = 0°$. Fig. 8 shows the optimal paths normalized by l, Fig. 9 shows $\overline{E}(t)$, Fig. 10 shows $\overline{V}_{err}(t)$, and Fig. 11 shows $\overline{A}(t)$ for three cases: $q/s = 1$ and $\beta = 0°$, $q/s = 1$ and $\beta = 45°$, and $q/s = 0.01$ and $\beta = 0°$. The path with $\beta = 45°$ was rotated using (6) so that the path's bisector was aligned with the x-axis.

Fig. 6 shows that as $A_0/A_{\max}$ decreases and θ is held constant, $V_{err,\max}$ decreases. While the velocity is fixed given deposition quality requirements and the maximum acceleration is fixed for a given machine, there is often flexibility in setting the leg length for long paths allowing for a decrease in velocity error using path planning alone. However, it should be noted that when fabricating fine features consisting of short paths, this flexibility is limited. As $A_0/A_{\max}$ decreases and θ is held constant, $E_{\max}$ increases and then decreases for most values of $\theta < 90°$ (see Fig. 7). In these regions, the optimal path is increasing the contour error cost to decrease the velocity error and acceleration costs. This can be seen in Fig. 8 for $\theta = 10°$ and $\beta = 0°$ where the path does not go as deep into the corner for $A_0/A_{\max} = 0.48$ as it does for $A_0/A_{\max} = 1.00$ or

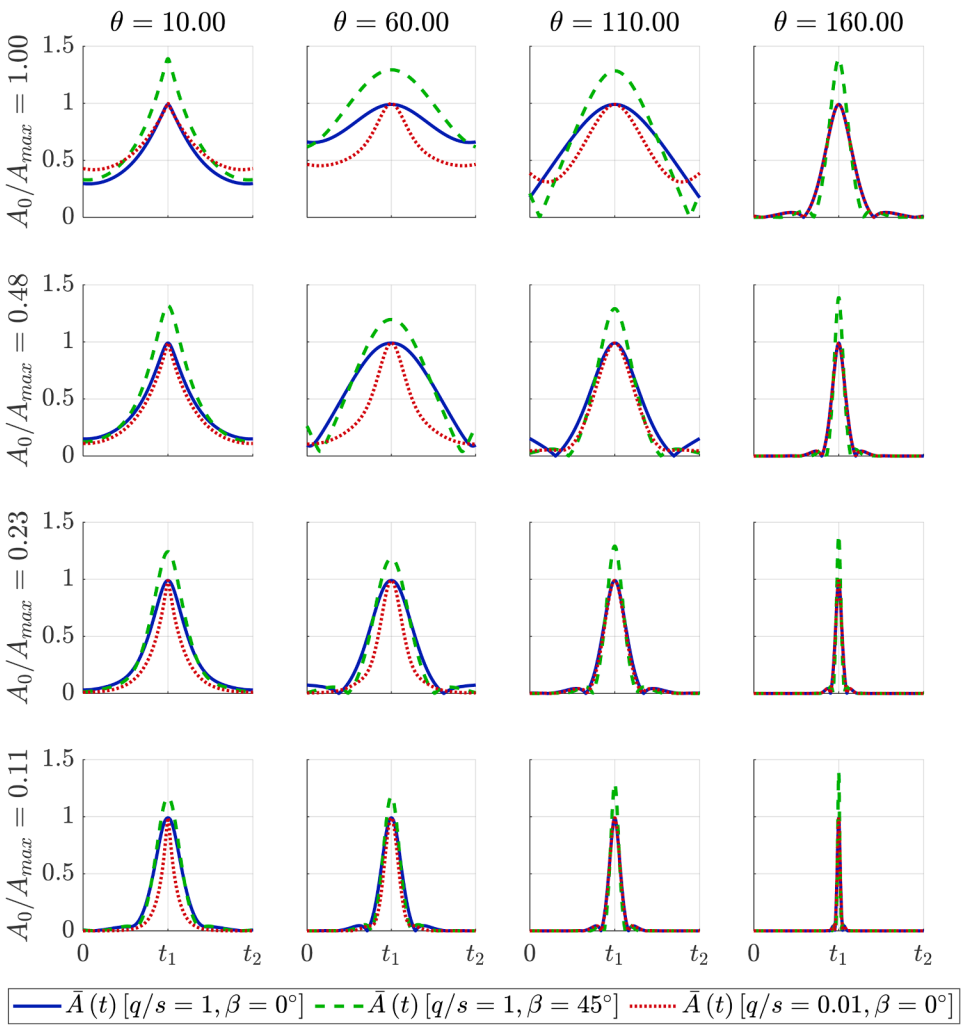

Fig. 11. Normalized acceleration profiles for various combinations of q/s and β.

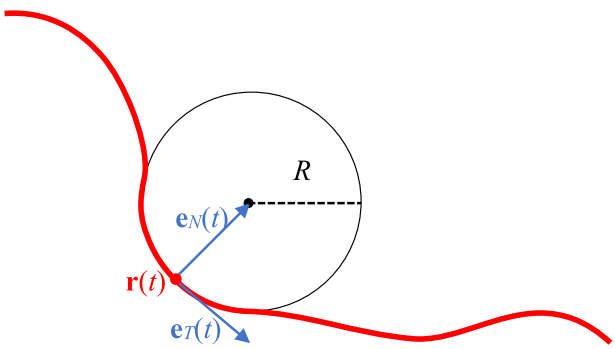

Fig. 12. Path with osculating circle.

0.23. Note that for other combinations of q/s and β the maximum contour error monotonically decreases as $A_0/A_{\max}$ decreases even for $\theta < 90°$. As θ approaches 180° and $A_0/A_{\max}$ is held constant, the values of $V_{err,\max}$, $E_{\max}$, $V_{err,\text{int}}$, and E_{int} approach 0. This is due to the fact that the optimal path approaches a straight line with constant velocity as θ approaches 180°. Note that for $\theta = 10°$ and large values of $A_0/A_{\max}$, the optimal solutions consist of looping paths. The exact values of θ and $A_0/A_{\max}$ at which this transition occur can be determined numerically.

The results in Figs. 8 and 9 show that as θ increases and $A_0/A_{\max}$ decreases the contour error decreases and the effects of q/s and β decrease. The one exception is $\theta = 10°$ where the contour error increases as $A_0/A_{\max}$ increases. This is an extreme case that is unlikely to be encountered in most additive manufacturing processes as the deposited material would substantially overlap at the corner when using such a narrow corner angle. The ratio $A_0/A_{\max}$ is decreased from 1.0 to 0.11 by increasing l from 1 to 10 mm. This illustrates the impact on contour error by adjusting l, which is the only parameter that may be adjusted since θ, V_0, and $A_{\max}$ are fixed given part design, part quality, and machine constraints, respectively. Most of the paths in Fig. 8 have rounded corners that stay inside the reference path or go slightly outside of the reference path (e.g., $\theta = 60°$, $A_0/A_{\max} = 0.11$, $q/s = 1$, and $\beta = 0°$) to generate path radii of curvature that is larger than would be possible if the path stayed inside the reference path. The solution shown in Fig. 8 with $\theta = 10°$, $A_0/A_{\max} = 1$, $q/s = 1$, and $\beta = 0°$ is a looping solution. Looping solutions occur when the acceleration needed to traverse the corner is large, i.e., when θ is small and $A_0/A_{\max}$ is large. Looping paths create significant material deposition off the reference path that would need to be removed in a subsequent manufacturing operation or may cause additional deposition at another section of the part. Further, looping paths cause the corner point to be fabricated twice, causing excessive buildup similar to a path that decelerates into, and accelerates out of, corners. Looping paths can be identified and, thus, avoided by examining the normal acceleration. When the normal acceleration is negative, the solution consists of a looping path and, thus, should be ignored.

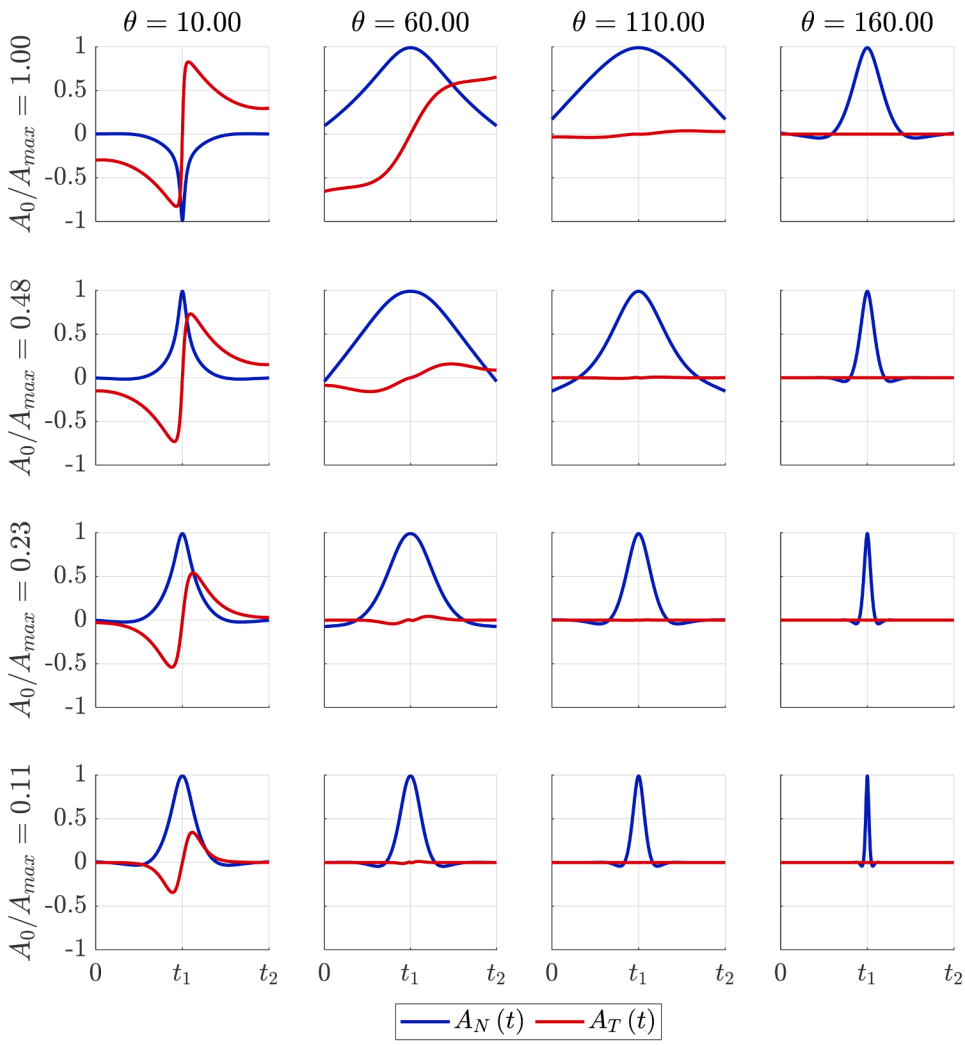

Fig. 13. Normal and tangential acceleration profiles for $q/s = 1$ and $\beta = 0°$.

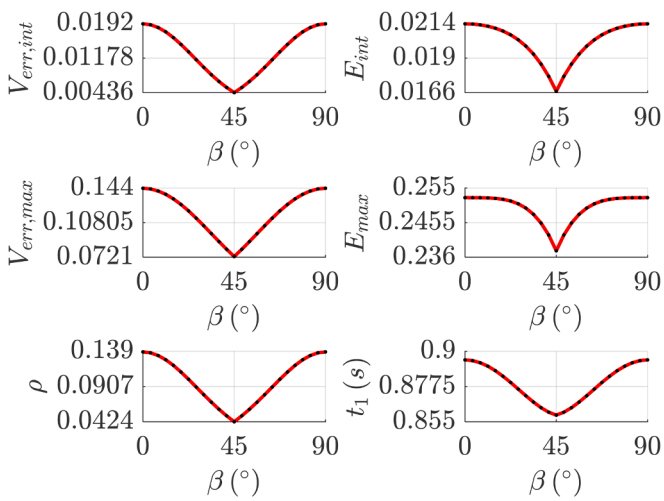

Fig. 14. Path errors, ρ, and t_1 as functions of β for $\theta = 90°$, $q/s = 1$, and $A_0/A_{\max} = 1$.

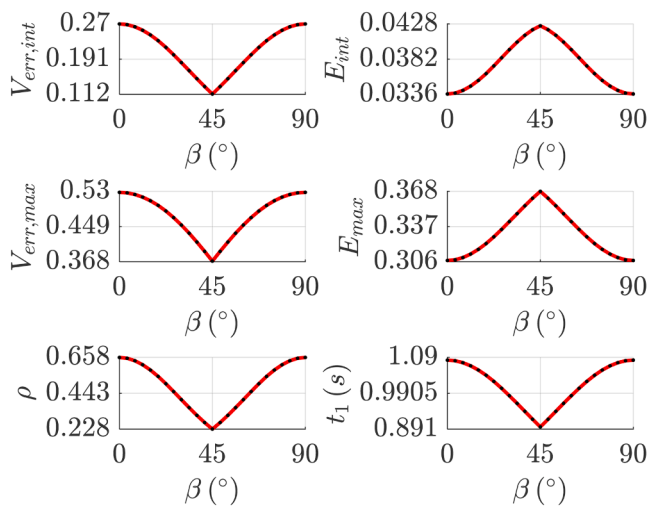

Fig. 15. Path errors, ρ, and t_1 as functions of β for $\theta = 60°$, $q/s = 1$, and $A_0/A_{\max} = 1$.

Fig. 10 illustrates that as $A_0/A_{\max}$ decreases and θ increases, the maximum velocity error and the integral of the velocity error decrease. Since the amount of acceleration needed to traverse the corner decreases as $A_0/A_{\max}$ decreases, the velocity error decreases. The amount of acceleration needed to change directions decreases when θ increases, leading to less velocity error. A smaller value of q/s assigns more

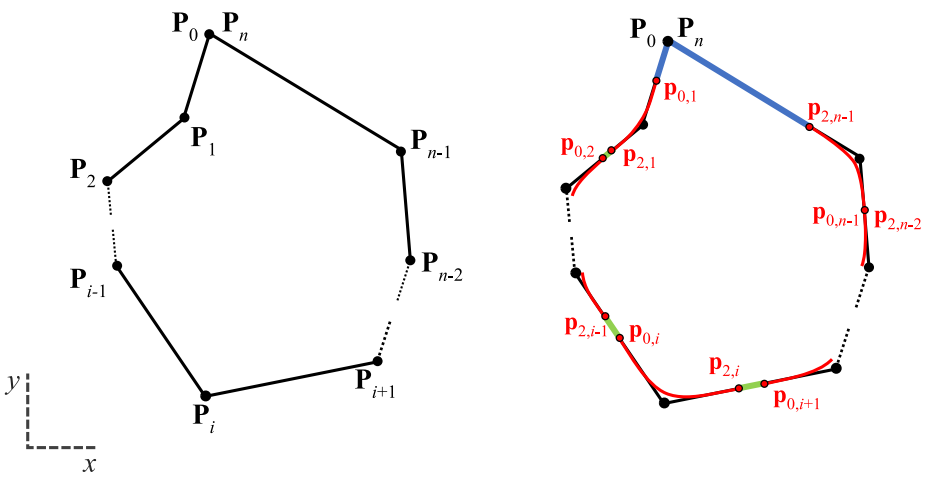

Fig. 16. Example path before (Left) and after (Right) optimization.

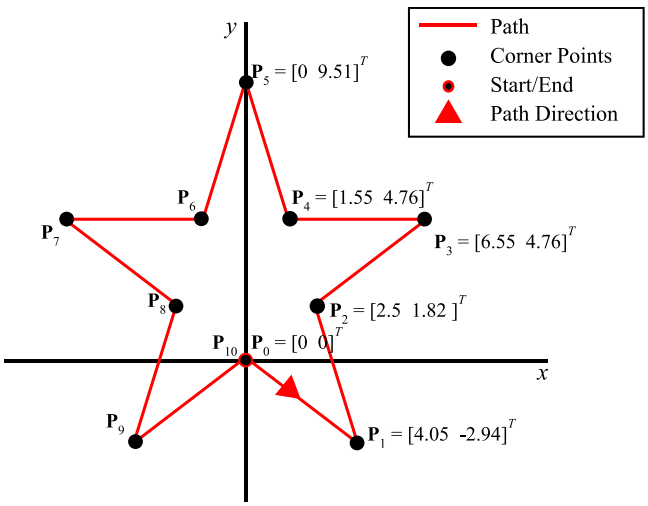

Fig. 17. Five-pointed star path.

emphasis on the contour error that, in turn, increases the velocity error. When $\beta \neq 0$, the path can take advantage of both the x-axis and y-axis maximum accelerations to decrease the velocity error. This difference is most noticeable for $\theta = 60^\circ$ and large values of $A_0/A_{\max}$; however, it is not noticeable for $\theta = 10^\circ$ since the corner is too narrow and for larger values of θ since the velocity errors are too small.

Fig. 11 shows normalized acceleration profiles for various combinations of θ and $A_0/A_{\max}$. All of the acceleration profiles have pulse-like shapes. As $A_0/A_{\max}$ decreases and θ increases, the amount of acceleration needed to generate the optimal path decreases since the corners become less sharp. When $\beta = 0^\circ$, $\max_t(A^-(t)) = 1$, occurring at t_1 and in the direction of the bisector, and $\max_t(A^-(t)) > 1$ when $\beta = 45^\circ$ because both axes contribute to the acceleration at this time, reaching a value of $\max_t(A^-(t)) = 2^{1/2}$. There is less acceleration when q/s is decreased as the optimal solution will seek a path with more velocity error and less contour error. The effect of q/s diminishes as θ increases because the need for acceleration at the corner diminishes to zero as the path approaches a straight line.

The total acceleration can be decomposed into normal and tangential components, which describe how much of the total acceleration is used to change direction and speed, respectively. The acceleration in terms of the normal and tangential vectors, denoted $\mathbf{e}_N(t)$ and $\mathbf{e}_T(t)$, respectively, is,

$$\ddot{\mathbf{r}}(t) = A_T(t)\mathbf{e}_T(t) + A_N(t)\mathbf{e}_N(t), \tag{46}$$

where the tangential and normal acceleration, respectively are,

$$A_T(t) = \frac{d}{dt}(\parallel \dot{\mathbf{r}}(t) \parallel) = \frac{\dot{\mathbf{r}}(t) \times \ddot{\mathbf{r}}(t)}{\parallel \dot{\mathbf{r}}(t) \parallel}, A_N(t) = \kappa(t)\parallel \dot{\mathbf{r}}(t) \parallel^2 = \frac{\dot{\mathbf{r}}(t)\cdot\ddot{\mathbf{r}}(t)}{\parallel \dot{\mathbf{r}}(t) \parallel}, \tag{47}$$

and the path's curvature is,

$$\kappa(t) = \frac{\det(\dot{\mathbf{r}}(t), \ddot{\mathbf{r}}(t))}{\parallel \dot{\mathbf{r}}(t) \parallel^3} = \frac{1}{R}, \tag{48}$$

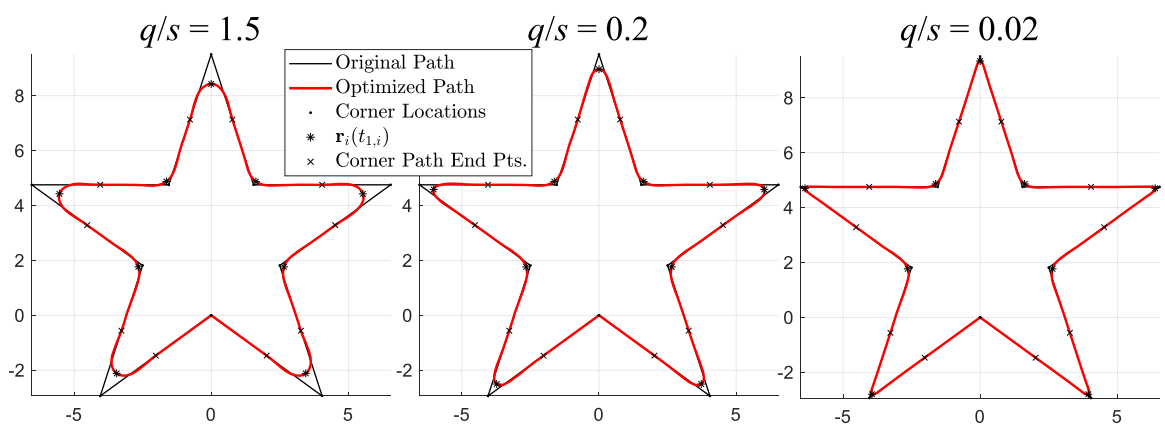

Fig. 18. Optimized star paths.

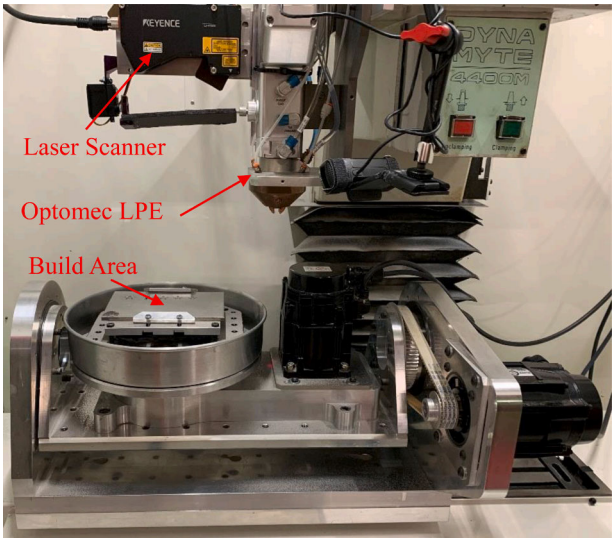

Fig. 19. Experimental DMD machine.

Table 1
Print parameters for star paths.

Parameter	Variable	Nominal value	Unit
Nominal Velocity	V_0	8.5	mm/s
Maximum Axes Acceleration	$A_{\max}$	100	mm/s^2
Laser Power	P	280	W

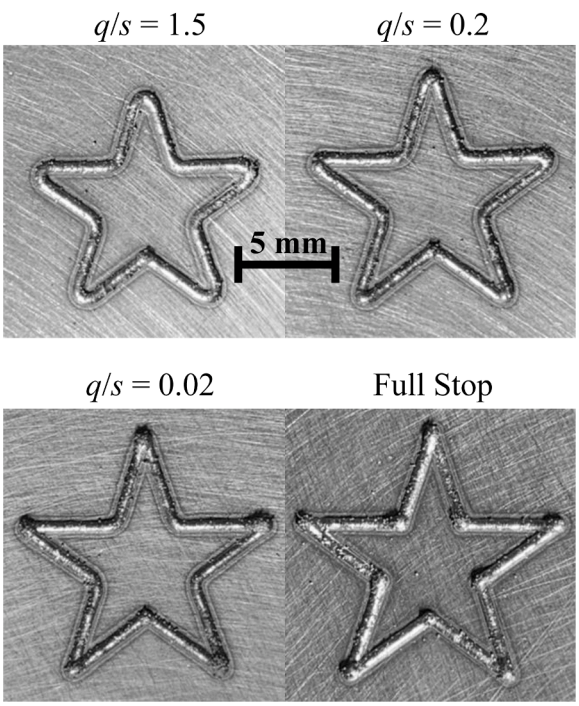

Fig. 20. Images of printed star paths.

where R is the radius of the osculating circle at $\mathbf{r}(t)$, as shown in Fig. 12. From (47), it is seen that smaller curvatures lead to smaller acceleration magnitudes. The magnitudes of $A_T(t)$, $A_N(t)$, and the curvature should be minimized to utilize the minimum amount of acceleration. The path should prefer allocating acceleration in the normal direction since acceleration in the tangential direction is related to velocity change.

Fig. 13 shows the normal and tangential acceleration profiles for $q/s = 1$ and $\beta = 0°$.

Fig. 13 shows that the magnitude of $A_T(t)$ decreases as $A_0/A_{\max}$ decreases and θ is held constant. The optimal path prefers using normal over tangential acceleration, since the latter is related to changes in the velocity magnitude. Tangential acceleration is mainly used when $A_0/A_{\max}$ is large and θ is small. The optimal path's curvature can be adjusted by looping, i.e., bulging outside of the reference path, or by curving sooner within the reference path. The normal acceleration becomes the dominant component as θ increases and $A_0/A_{\max}$ decreases, and the acceleration approaches a true pulse profile. Note that for situations where the path loops, the normal acceleration is negative.

Letting $\theta = 90°$, $q/s = 1$, and $A_0/A_{\max} = 1$ by setting $V_0 = A_{\max} = l = 1$ in respective units, and varying β using 25 linearly spaced points, the optimal paths were found and $V_{err,\max}$, $E_{\max}$, $V_{err,\text{int}}$, E_{int}, ρ, and t_1 were plotted as functions of β in Fig. 14. Note that β is constrained to the range [0°, 90°] due to geometry.

Fig. 14 shows that the functions for $V_{err,\max}$, $E_{\max}$, $V_{err,\text{int}}$, E_{int}, ρ, and t_1 are symmetric about $\beta = 45°$. When $\beta = 0°$ or 90°, the maximum acceleration is aligned with either the x or y axis and the optimal path has maximum $V_{err,\max}$ and $V_{err,\text{int}}$ with respect to β. When $\beta = 45°$, the optimal path has minimal $V_{err,\max}$ and $V_{err,\text{int}}$ with respect to β. As β increases from 0° to 45°, the maximum allowable total normalized acceleration increases from 1 to $2^{1/2}$ because the path can maximize the accelerations of both the x and y axes, providing lower velocity error. One might assume that higher accelerations correspond to lower contour errors; however, this is not the case because, unlike the velocity error, the contour error is not directly related to the acceleration. In Fig. 15, the path errors for $\theta = 60°$, $q/s = 1$, and $A_0/A_{\max} = 1$ were generated over the same range of β. When $\theta = 60°$, the contour errors are maximum when $\beta = 45°$ and minimum when $\beta = 0°$ or 90°. The difference in contour error behavior for different values of θ is most likely related to the path curvature and how the optimal path allocates its acceleration in the normal and tangential directions. From Fig. 15, it can be seen that the solution for $\theta = 60°$, $q/s = 1$, and $A_0/A_{\max} = 1$ is different than the solutions for the other cases in that the contour error increases as β increases. This may be due to the fact that the acceleration is large and a looping solution is being approached as θ decreases. For both Figs. 14 and 15, the value of t_1 decreases as β increases from 0° to 45° due to the higher accelerations that are possible.

3. Experiments

3.1. Application of corner smoothing methodology to straight-line paths

To optimize a tool path which uses only straight-line motions, the following process is employed. First, each corner point in the path is extracted and denoted $\mathbf{P}_i = [x_i\, y_i]^T$, where $i = 0,1,\ldots,n$ indicates the order of the corner points along the path. The tool path is broken into corner sections and linear sections. Corner sections are local areas around each corner point which have optimal corner paths fit to them. Corner sections are connected with linear sections, i.e., straight line motions which have a constant commanded velocity profile. Entering the first corner section is a linear section with a commanded trapezoidal velocity profile starting from rest and accelerating at $A_{\max}$ to V_0. Exiting the last corner section is a similar linear section starting at V_0 and decelerating at $A_{\max}$ to rest. Fig. 16, below, shows an example path before and after it is optimized.

In Fig. 16, corner sections are defined for $i = 1,2,\ldots,n$-1 and are shown in red. Connecting the corner sections together are constant velocity linear sections, shown as green lines. The first and last linear sections, which have trapezoidal velocity profiles, are shown as blue lines. The red points are added to the path to define the endpoints of the corner sections and are given by,

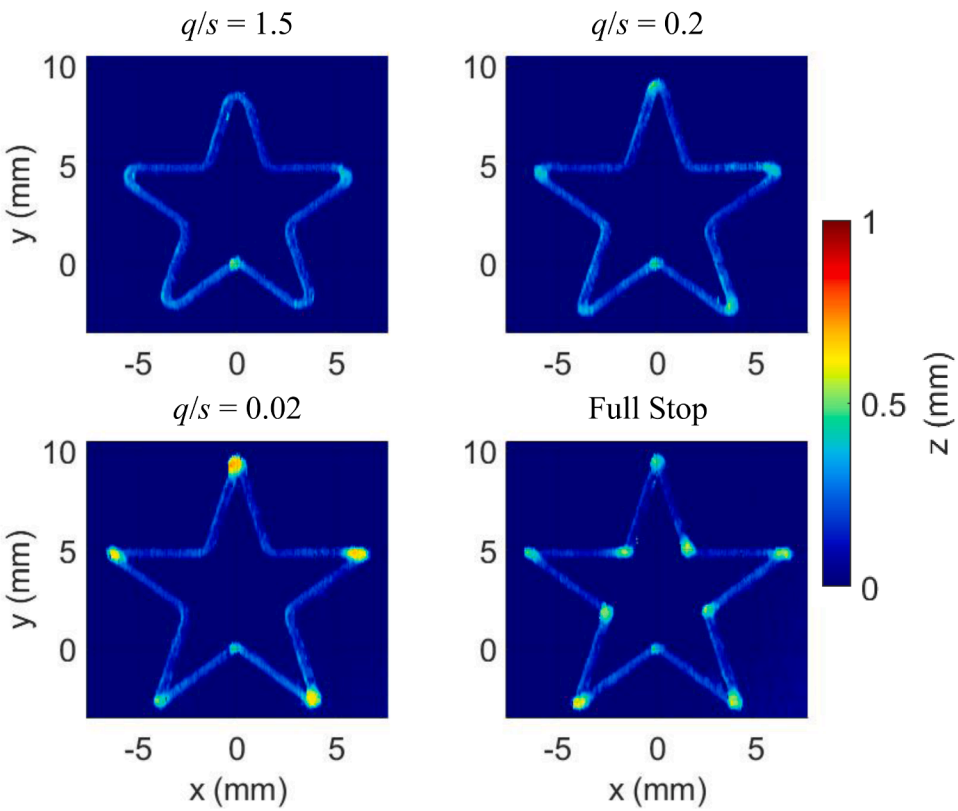

Fig. 21. Laser scans of printed star paths.

$$\mathbf{p}_{0,i} = \mathbf{P}_i + \frac{\min(l_{i-1}, l_i)}{2}\mathbf{e}_{1,i},$$
$$\mathbf{p}_{2,i} = \mathbf{P}_i + \frac{\min(l_{i-1}, l_i)}{2}\mathbf{e}_{2,i}. \tag{49}$$

where $\mathbf{e}_{1,i} = [\cos(\theta_{1,i})\ \sin(\theta_{1,i})]^T$, $\mathbf{e}_{2,i} = [\cos(\theta_{2,i})\ \sin(\theta_{2,i})]^T$, and l_i is the Euclidian distance between $\mathbf{P}_i$ and $\mathbf{P}_{i+1}$. The corner region angles are,

$$\theta_{1,i} = \tan^{-1}(y_{i-1} - y_i, x_{i-1} - x_i),$$
$$\theta_{2,i} = \tan^{-1}(y_{i+1} - y_i, x_{i+1} - x_i). \tag{50}$$

The optimal corner path between $\mathbf{p}_{0,i}$ and $\mathbf{p}_{2,i}$ is denoted $\mathbf{r}_i(t_i)$ with initial, mid-point, and final times of $t_{0,i}$, $t_{1,i}$, and $t_{2,i}$, respectively. A B-spline is fit to each path $\mathbf{r}_i(t_i)$ using the NURBS fitting process developed in [14].

After the corner sections are defined, the linear sections, which have a constant commanded velocity and connect consecutive corner sections, are defined. Constant velocity linear paths are defined between $i = 1$ and $i = n$-1 with,

$$\mathbf{L}_i(t) = \mathbf{p}_{2,i} + V_0 t\mathbf{e}_{2,i}, t \in \left[0, \frac{l_{L,i}}{V_0}\right]. \tag{51}$$

where $l_{L,i} = \| \mathbf{p}_{0,i+1} - \mathbf{p}_{2,i} \|$. If $l_{L,i}$ is too small, i.e., $l_{L,i} \leq V_0\Delta t$ where Δt is the machine controller time-step, the corner sections are connected. The first and last linear sections, i.e., the sections connecting $\mathbf{P}_0$ to $\mathbf{p}_{0,1}$, and $\mathbf{p}_{2,n\text{-}1}$ to $\mathbf{P}_n$, have trapezoidal velocity profiles fit to them.

3.2. Direct metal deposition (DMD) printing experiments

A five-pointed star path was used to experimentally test the corner smoothing methodology. The star path is a regular five-pointed star with side lengths of 5 mm. Fig. 17 shows the star path and half of the corner point locations.

Three different optimized paths were created, each with a different q/s value. These values were found by calculating the optimal path starting with $q/s = 1$ and then adjusting the ratio until the velocity error was less than a certain value. Values of $q/s = 1.5$, 0.2, and 0.02 were chosen for $\bar{V}_{err,\max} \leq 25\%$, $\bar{V}_{err,\max} \leq 50\%$, and $\bar{V}_{err,\max} \leq 75\%$, respectively. To compare the proposed method to a pre-existing path planning method, a full-stop version of the path was also created. The full-stop method commanded the path to come to a complete stop at each corner point, giving 100% velocity error and 0% contour error at each corner. The full-stop path uses trapezoidal velocity profiles for each line segment connecting the corner points.

A B-spline with 16 control points was fit to each path $\mathbf{r}_i(t_i)$ using the NURBS fitting process developed in [14]. The number of control points was chosen such that the values of

$$\Delta V_{err,\max}\% = \left| \max_t \left[\frac{|\dot{\mathbf{b}}_i(t_i) - \mathbf{r}_i(t_i)|}{V_0} \right] \right| \times 100\% \tag{52}$$

and

$$\Delta V_{\text{int}}\% = \frac{\int \left[\frac{\dot{\mathbf{b}}_i(t_i) - \mathbf{r}_i(t_i)}{V_0} \right]^2 dt}{\int dt} \times 100\% \tag{53}$$

were less than 1% and 0.5% respectively, and $\mathbf{b}_i(t_i)$ is the B-spline fit to path $\mathbf{r}_i(t_i)$. Fig. 18 shows the optimized paths. Note that $l_{i\text{-}1} = l_i$ for all $i \in \{1,2, \ldots,9\}$, i.e., there are no linear sections with constant velocity connecting each corner path and $\mathbf{p}_{2,i\text{-}1} = \mathbf{p}_{0,i}$ for all i. This will make $A_0/A_{\max}$ as small as possible and allow the smoothing methodology to make larger tradeoffs between the velocity and contour errors by changing q/s.

Each path was printed using a DMD 3D printing machine, comprised of a CNC machine customized with an Optomec LENS Print Engine (LPE). The LPE is composed of a dual-hopper Optomec powder feeder system, an IPG YLR-1000-MM 1 kW fiber laser, and a cladding head which contains the routing for the powder and the laser fiber. After

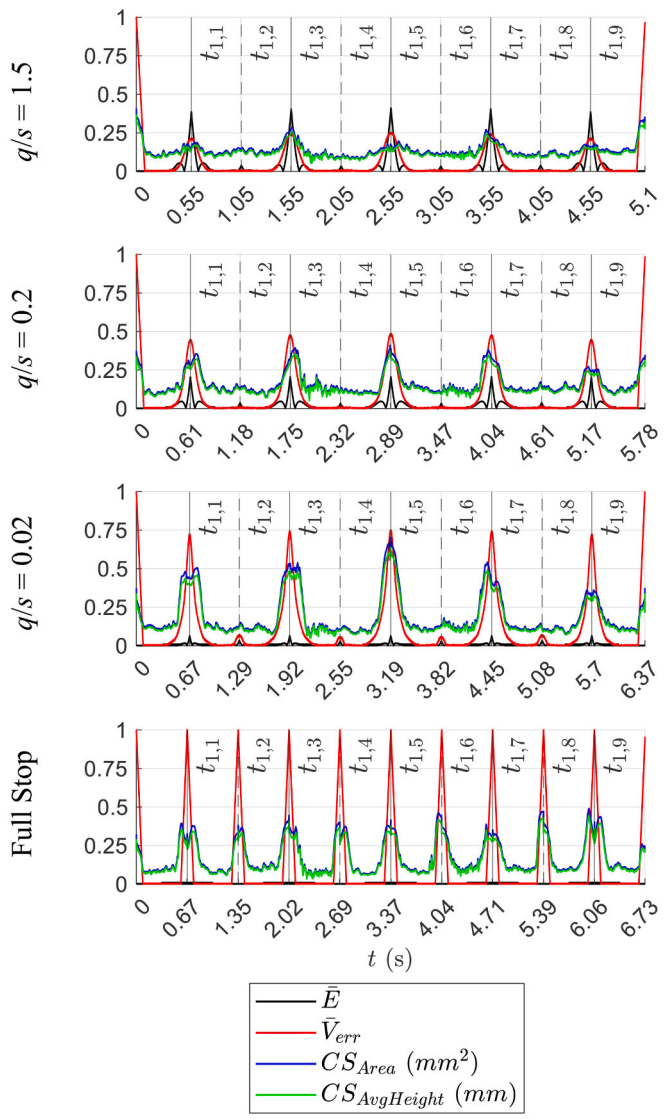

Fig. 22. Printed star path contour error, velocity error, cross-sectional area, and average height.

printing, the deposited path was measured using a Keyence LJ-V7200 laser line scanner, which has a linewidth of 62 mm and a resolution of 5 μm. Fig. 19 shows an image of the printing machine. The printing parameters used for the test prints are summarized in Table 1. Fig. 20 shows images of each printed path and Fig. 21 shows the laser scans of each printed path.

The cross-sectional area and average height were calculated by taking a plane cross-section normal to the velocity vector at each location in the printed path. In order to exclude the substrate from the morphology calculations, a datum plane was fit to the substrate. The absolute velocity error integral and the absolute contour error integral are defined, respectively, by

$$V_{err,\text{absint}} = \int_{t_i}^{t_f} |\overline{V}_{err}(t)| dt, \tag{54}$$

and

$$E_{\text{absint}} = \int_{t_i}^{t_f} |\overline{E}(t)| dt, \tag{55}$$

where $\bar{V}_{err}(t)$ is the normalized velocity error, $\bar{E}(t)$ is the normalized contour error, and t_i and t_f are the path start and the end times, respectively. Denoting the cross-sectional area with respect to time by $CS_{Area}(t)$, the absolute integral measure is,

$$CS_{Area,\text{absint}} = \int_{t_i}^{t_f} |CS_{Area}(t)| dt. \tag{56}$$

Lastly, the cross-sectional average height with respect to time is denoted $CS_{AvgHeight}(t)$. The functions $CS_{Area}(t)$, $CS_{AvgHeight}(t)$, $\bar{E}(t)$, and $\bar{V}_{err}(t)$ were calculated and plotted for each path and are shown in Fig. 22. The turning point time $t_{1,i}$ of each optimized corner is marked with a vertical line. Note that the time $t_{1,i}$ corresponds to when the print path is closest to $\mathbf{P}_i$ and that larger q/s values correspond to less emphasis on velocity error and more emphasis on contour error.

Fig. 22 shows that the cross-sectional area and average height were larger when there is more velocity error. The effect of velocity error on the morphology measures is shown in greater detail in Fig. 23, which is a zoomed view of the velocity error, contour error, and morphology measures of corners 1 and 2. Note that corner 1 is acute with $\theta = 36°$, and corner 2 is obtuse with $\theta = 108°$. Acute-angled corners have higher velocity error than the obtuse-angled corners, leading to more material buildup (see Fig. 6).

In Fig. 23 there is no noticeable variation in the morphology measures when the maximum velocity error is under 25%. However, there are very clear differences in morphology measures between the obtuse and acute corners in all optimized prints due to the difference in $V_{err,\text{abs int}}$. Between each respective acute/obtuse corner in the optimized prints, there are small differences in $V_{err,\text{abs int}}$ due to differences in β. When full stop is used, it generates a similar amount of deposited material at all corners since every corner has the same $V_{err,\text{abs int}}$ value regardless of θ. Fig. 24 shows the absolute integral of the scanned areas of the acute angles as a function of their corresponding absolute integral of velocity errors. Obtuse corners were excluded from Fig. 24 because their velocity error was not large enough to cause significant variation in the morphology measures. The amount of deposited material is governed by conservation of mass and, thus, the volumetric rate of deposition and part morphology depend on the powder catchment efficiency, material feed rate, and path velocity. Assuming powder catchment efficiency and material feed rate are constant, the deposited volume will strongly depend on the velocity in a linear manner. Indeed, a strong linear correlation between $V_{err,\text{abs int}}$ and $CS_{area,\text{abs int}}$ is seen in Fig. 24. The linear trend has a positive slope since the machine decelerates into, and accelerates out of, each corner causing the velocity to decrease and extra material to be deposited. The distinct groups of data points in Fig. 24 correspond to each print: $q/s = 1.5$ is grouped around $V_{err,\text{abs int}} = 0.04$, full stop and $q/s = 0.2$ are grouped around $V_{err,\text{abs int}} = 0.08$, and $q/s = 0.02$ is grouped around $V_{err,\text{abs int}} = 0.12$. As the ratio of q/s increases, the velocity error and, thus, morphology errors decrease. While the maximum velocity error for prints with $q/s = 0.02$ is not as large as the maximum velocity error for prints with full stop, the integral of the velocity error is larger, causing larger morphology errors.

Another point to note in Fig. 23 is that two peaks occur at acute angled corners. The two peaks are a result of the area calculation process, which was conducted by taking a plane cross-section normal to the velocity vector at each location along the printed path. Fig. 25 shows the location of the cross-section measurement plane at three different times. When the velocity direction changes rapidly, so does the cross-section plane, causing the measurements to change. At t_a the measurement plane is entering the bead at the corner and the cross-section measurements begin to increase. At t_b, the cross-section measurements reach a plateau as the plane begins to turn. The dip is greatest at the turning point of acute angled paths, or t_c in Fig. 25, because that is where the angle of the measurement plane is changing most rapidly. The dip is even more noticeable at the turning points in the full stop print because

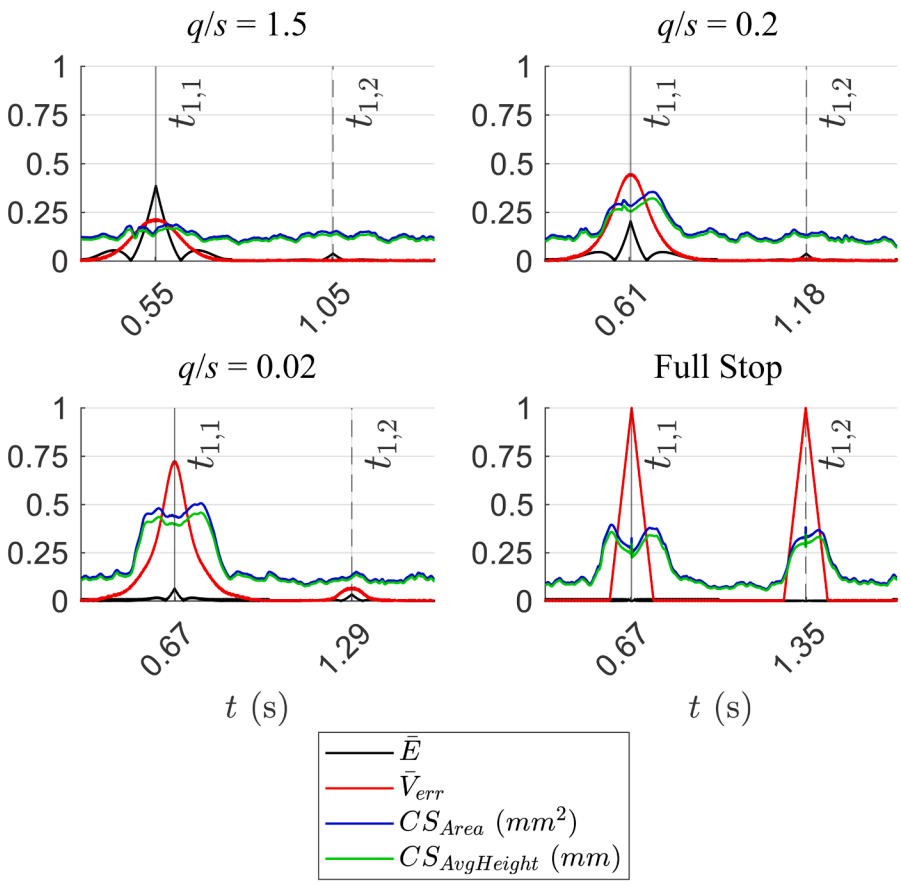

Fig. 23. Star path contour error, velocity error, cross-sectional area, and average height of corners 1 and 2.

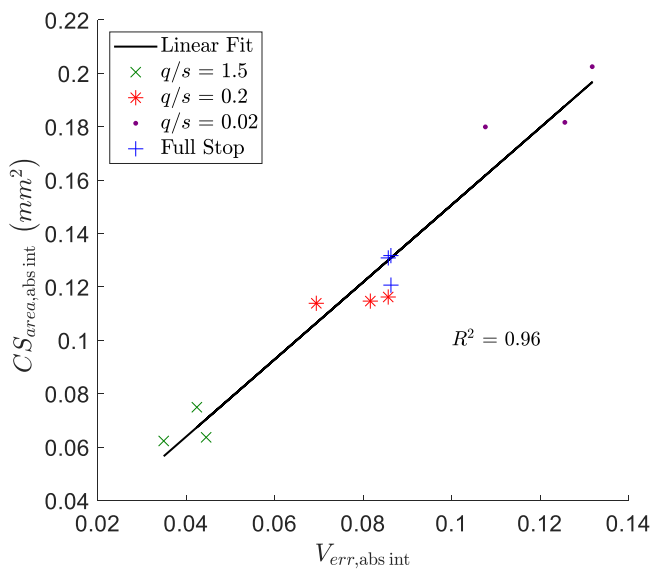

Fig. 24. Star path $CS_{area,\text{abs int}}$ versus $V_{err,\text{abs int}}$ for acute corners.

the velocity direction changes instantaneously at the corners.

The mean and standard deviation of both morphology measures, $V_{err,\text{abs int}}$, $E_{\text{abs int}}$, $V_{err,\max}$, and $E_{\max}$ for each star path was calculated for 31,847 points along all of the print paths and can be seen in Table 2. Optimized prints with $q/s = 1.5$ and $q/s = 0.2$ have smaller means and less variation in the morphology measures than the full stop print. This was because the optimized prints have significantly less velocity error at the cost of more contour error. However, even though the print with $q/s = 0.02$ had less maximum velocity error, the morphology measures had higher means and variations than those for the full stop print. This is due to the fact that even though the velocity errors at the obtuse angles are much smaller for the print with $q/s = 0.02$ than for the full stop print, the velocity errors and, hence, the morphology errors were much worse at the acute angles. To illustrate this, Table 3 shows the $V_{err,\text{abs int}}$ measures for the corners of the star path. Equal and opposite corners about the y-axis have the same performance, i.e., corners 1, 2, 3, and 4 perform the same as corners 6, 7, 8, and 9, respectively, and, thus, the data for the latter corners are not given. Table 3 shows that the values of $V_{err,\text{abs int}}$ at the acute angled corners were larger for the print with $q/s = 0.02$ than for the full stop print. For prints with $q/s = 1.5$ and $q/s = 0.2$, acute angled corners had smaller values of $V_{err,\text{abs int}}$ than that for the full stop print, thus, the machine slowed down too much at those corners to improve performance. There was an improvement in the morphology measures at all of the obtuse-angled corners of the optimized prints due to the decrease in $V_{err,\text{abs int}}$.

Simulation studies were conducted for $0.01 \leq q/s \leq 5$ and the resulting final times are shown in Fig. 26 and the resulting velocity and contour errors are shown Fig. 27. For the full stop path, the final time was 6.73 s. The optimized prints with $q/s = 1.5$, 0.2, and 0.02 decreased the final time by 24%, 14%, and 5%, respectively. The corner smoothing methodology decreases the final time by reducing the amount of velocity error (i.e., not slowing down at the corners) at the expense of increased contour error. As q/s decreases the solution approaches the full stop path where the velocity errors will be their maximum values and the contour errors will approach zero. It should be noted that while the contour error is zero for the full stop path, the motion system will decelerate and accelerate into and out of, respectively, the corner, which will create excess deposition. As q/s increases it appears the solution will generate a

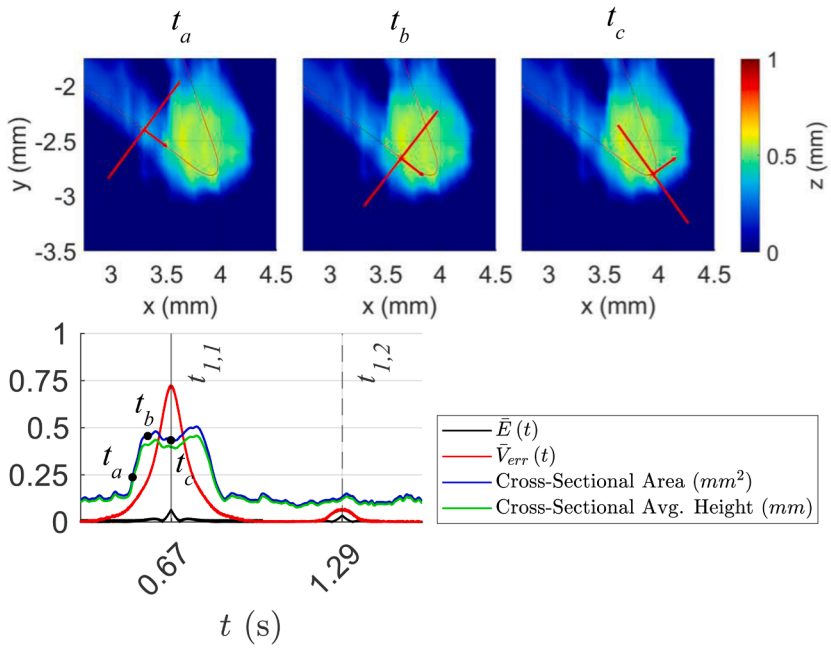

Fig. 25. Star path cross-section plane location at various times for $q/s = 0.02$.

Table 2
Velocity and contour errors and mean morphology measures of printed star paths.

Print	$V_{err,\text{abs int}}$	$V_{err,\max}$	$E_{\text{abs int}}$	$E_{\max}$	CS_{Area} (mm^2) Mean	Std. dev.	$CS_{AvgHeight}$ (mm) Mean	Std. dev.	Final time (s)
$q/s = 1.5$	0.291	0.247	0.175	0.411	0.139	4.55×10^{-2}	0.125	4.11×10^{-2}	5.10
$q/s = 0.2$	0.482	0.483	0.112	0.206	0.165	7.49×10^{-2}	0.149	6.79×10^{-2}	5.78
$q/s = 0.02$	0.710	0.742	4.21×10^{-2}	6.45×10^{-2}	0.194	0.140	0.175	0.127	6.37
Full Stop	0.861	1.00	0	0	0.179	0.115	0.162	0.104	6.73

Table 3
Absolute velocity error integral of first five corners of printed star paths.

i	θ (°)	β (°)	$V_{err,\text{ abs int}}$ $q/s = 1.5$	$q/s = 0.2$	$q/s = 0.02$	Full stop
1	36	126	3.49×10^{-2}	6.93×10^{-2}	0.107	8.50×10^{-2}
2	108	−18	1.05×10^{-4}	7.70×10^{-4}	6.50×10^{-3}	8.50×10^{-2}
3	36	18	4.24×10^{-2}	8.16×10^{-2}	0.125	8.50×10^{-2}
4	108	54	4.13×10^{-5}	5.27×10^{-4}	4.60×10^{-3}	8.50×10^{-2}
5	36	−90	4.46×10^{-2}	8.57×10^{-2}	0.1315	8.50×10^{-2}

path where the corners are rounded, possibly a circle, such that the velocity errors will be nearly zero and the contour errors and final time will approach constant values. This conjecture cannot be validated at this time due to numerical issues encountered when solving the optimization problem for large values of q/s.

4. Summary and conclusions

A trajectory smoothing method for additive manufacturing processes which allows the user to systematically trade-off velocity and contour errors at corners was presented. The trajectory planning problem is posed as an optimal control problem for a constrained dynamic system that is numerically solved as a boundary value problem. It was found that when the acceleration entering the corner was large or the corner angle was small, velocity and contour errors increased until the optimal solution consisted of a looping solution. Also, the corner leg length should be made as large as possible, given part geometry constraints (e.g., one half the segment length), to decrease the acceleration entering the corner and, thus, the velocity and contour errors. Experiments were

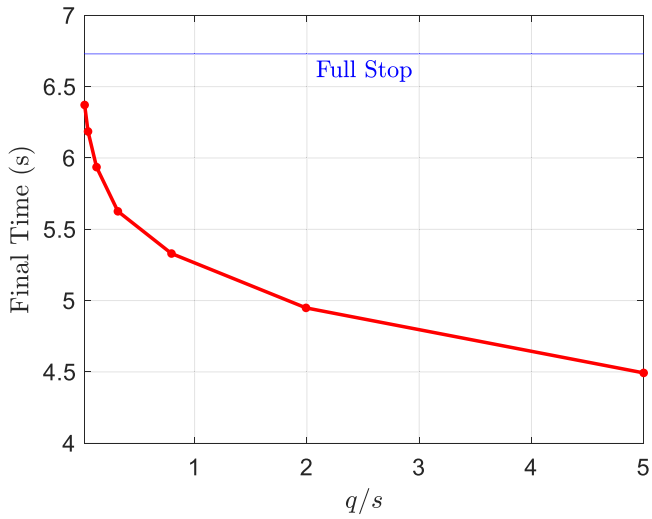

Fig. 26. Optimized star path final time as function of q/s.

conducted to fabricate a star with an acute angle and an obtuse angle and the material area and height, in addition to velocity and contour errors, were measured. These experiments consisted of three values of q/s and were compared to an experiment where the machine came to a full stop at the corners. It was found that the corners with the acute angle had substantially more velocity and morphological errors as compared to corners with the obtuse angle. Also, as q/s increased (i.e., velocity error was weighted more heavily), the velocity and morphological errors

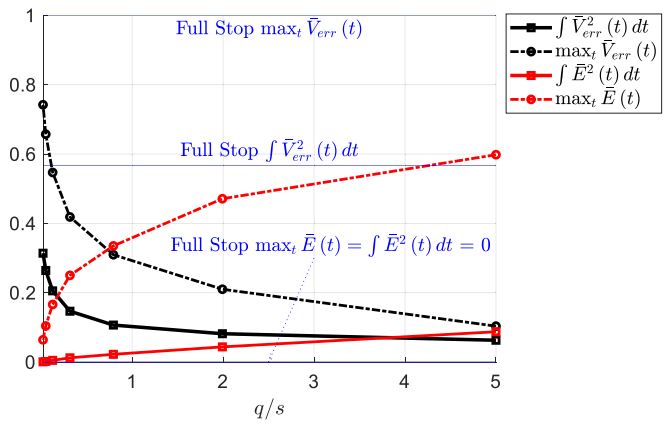

Fig. 27. Optimized star path velocity error and contour error measures as functions of q/s.

at the corners, in addition to the final time, decreased exponentially towards a constant value while the contour error increased exponentially towards a constant value. As q/s decreased, the results approached those of the full stop experiment.

CRediT authorship contribution statement

Emilio Perez: Methodology, Software, Validation, Formal analysis, Investigation, Writing – review & editing, Visualization. **Robert Landers:** Conceptualization, Methodology, Methodology, Validation, Formal analysis, Writing – review & editing. **Douglas Bristow:** Conceptualization, Methodology, Methodology, Validation, Formal analysis, Writing – review & editing, Supervision, Project administration, Supervision.

Declaration of Competing Interest

None

Appendix: Iterative ρ-solver

To find the value of ρ such that (19) is met, an iterative solver was created. Note that as ρ is increased or decreased, the maximum acceleration is decreased or increased, respectively. By wrapping *bvp4c* in a while loop and calculating the optimal path every iteration, an update law for ρ can be written,

$$\rho_{i+1} = \frac{A_i}{A_{\max}}\rho_i, \tag{57}$$

where i represents the iteration number, ρ_i is the value of ρ at iteration i, and

$$A_i = \max\left(\max_t\left(\ddot{x}_i(t)\right), \max_t\left(\ddot{y}_i(t)\right)\right), \tag{58}$$

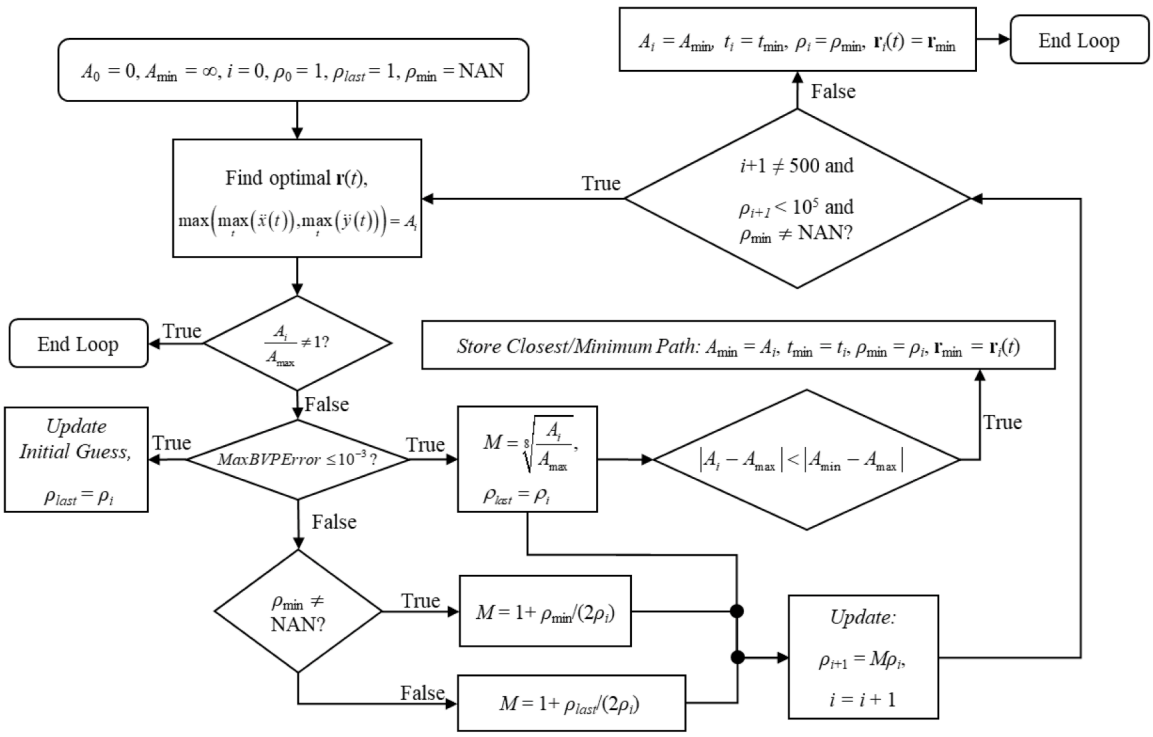

Fig. 28. ρ-solver block diagram.

where $\mathbf{r}_i(t) = [x_i(t)\ y_i(t)]^T$ is the optimal path found at the current iteration. However, *bvp4c* is a numerical solver and sometimes has issues finding a solution which matches the boundary conditions provided or that satisfy the error tolerance criteria. For this reason, extra checks were added to the solver. First, the value $\rho_{\min}$ is defined as,

$$\rho_{\min} = \underset{\rho_k \in P}{\operatorname{argmin}} \left| \frac{A_i}{A_{\max}} - 1 \right|, \tag{59}$$

where $P = \{\rho_0, \rho_1, \ldots, \rho_i\}$. The value of $A_{\min}$ is the corresponding value of (58) when $\rho_{\min}$ is used to find the optimal path. The maximum *bvp4c* residual error was assigned to a variable "*MaxBVPError*". The maximum number of iterations is 500. The loop is initialized with $i = 0$, $A_0 = 0$, $A_{\min} = \infty$, $\rho_{last} = 1$, and $\rho_{\min} = \text{NAN}$. The solver uses three different update equations depending on the values of *MaxBVPError* and $\rho_{\min}$. If $MaxBVPError \leq 10^{-3}$, then

$$\rho_{i+1} = 8\sqrt{\frac{A_i}{A_{\max}}}\rho_i. \tag{60}$$

Along with updating ρ, the value of the most recent value of ρ, denoted ρ_{last}, is updated to ρ_i and the initial guess is updated to $\mathbf{r}_i(t)$. Eq. (60) is used instead of (57) because the radical slows down the update rate so that possible solutions are not missed. If $MaxBVPError > 10^{-3}$ and $\rho_{\min} \neq \text{NAN}$, then

$$\rho_{i+1} = \frac{\rho_i + \rho_{\min}}{2}. \tag{61}$$

Lastly, if $MaxBVPError > 10^{-3}$ and $\rho_{\min} = \text{NAN}$, then

$$\rho_{i+1} = \frac{\rho_i + \rho_{last}}{2}. \tag{62}$$

A block structure of the ρ-Solver is shown in Fig. 28.

References

[1] Ding D, Pan Z, Cuiuri D, Li H. A practical path planning methodology for wire and arc additive manufacturing of thin-walled structures. Robot Comput Integr Manuf 2015;34:8–19. https://doi.org/10.1016/j.rcim.2015.01.003.

[2] Ding D, Pan Z, Cuiuri D, Li H, Larkin N. Adaptive path planning for wire-feed additive manufacturing using medial axis transformation. J Clean Prod 2016;133: 942–52. https://doi.org/10.1016/j.jclepro.2016.06.036.

[3] an Jin Y, Y He, zhong Fu J, feng Gan W, wei Lin Z. Optimization of tool-path generation for material extrusion-based additive manufacturing technology. Addit Manuf 2014;1:32–47. https://doi.org/10.1016/j.addma.2014.08.004.

[4] Xie F, Chen L, Li Z, Tang K. Path smoothing and feed rate planning for robotic curved layer additive manufacturing. Robot Comput Integr Manuf 2020;65: 101967. https://doi.org/10.1016/j.rcim.2020.101967.

[5] Ertay DS, Yuen A, Altintas Y. Synchronized material deposition rate control with path velocity on fused filament fabrication machines. Addit Manuf 2018;19: 205–13. https://doi.org/10.1016/j.addma.2017.05.011.

[6] Han W, Jafari MA. Coordination control of positioning and deposition in layered manufacturing. IEEE Trans Ind Electron 2007;54:651–9. https://doi.org/10.1109/TIE.2006.885468.

[7] Giberti H, Sbaglia L, Urgo M. A path planning algorithm for industrial processes under velocity constraints with an application to additive manufacturing. J Manuf Syst 2017;43:160–7. https://doi.org/10.1016/j.jmsy.2017.03.003.

[8] Comminal R, Serdeczny MP, Pedersen DB, Spangenberg J. Motion planning and numerical simulation of material deposition at corners in extrusion additive manufacturing. Addit Manuf 2019;29:100753. https://doi.org/10.1016/j.addma.2019.06.005.

[9] Ernesto CA, Farouki RT. High-speed cornering by CNC machines under prescribed bounds on axis accelerations and toolpath contour error. Int J Adv Manuf Technol 2012;58:327–38. https://doi.org/10.1007/s00170-011-3394-3.

[10] Imani BM, Jahanpour J. High-speed contouring enhanced with P-H curves. Int J Adv Manuf Technol 2008;37:747–59. https://doi.org/10.1007/s00170-007-1006-z.

[11] Erkorkmaz K, Yeung C-H, Altintas Y. Virtual CNC system. Part II. High speed contouring application. Int J Mach Tools Manuf 2006;46:1124–38. https://doi.org/10.1016/j.ijmachtools.2005.08.001.

[12] Bosetti P, Bertolazzi E. Feed-rate and trajectory optimization for CNC machine tools. Robot Comput Integr Manuf 2014;30:667–77. https://doi.org/10.1016/j.rcim.2014.03.009.

[13] Mercy T, Jacquod N, Herzog R, Pipeleers G. Spline-based trajectory generation for CNC machines. IEEE Trans Ind Electron 2019;66:6098–107. https://doi.org/10.1109/TIE.2018.2874617.

[14] Duan M, Okwudire C. Minimum-time cornering for CNC machines using an optimal control method with NURBS parameterization. Int J Adv Manuf Technol 2016;85: 1405–18. https://doi.org/10.1007/s00170-015-7969-2.

Emilio Perez graduated in 2021 from the Missouri University of Science and Technology with a M.S. degree in Mechanical Engineering. He is currently working as a Software Developer for Ushr Inc. His research interests are in additive manufacturing and in the path planning and control of manufacturing equipment.

Dr. Robert G. Landers is the Advanced Manufacturing Collegiate Professor in the Department of Aerospace and Mechanical Engineering at the University of Notre Dame. He was previously a Curators' Distinguished Professor at the Missouri University of Science and Technology and served for three years as a program manager at the National Science Foundation. He received his Ph.D. degree in Mechanical Engineering from the University of Michigan in 1997. His research interests are in the areas of modeling, analysis, monitoring, and control of manufacturing processes, volumetric error compensation of manufacturing equipment, and in the estimation and control of lithiumion batteries and hydrogen fuel cells. He received the Society of Manufacturing Engineers' Outstanding Young Manufacturing Engineer Award in 2004, the ASME Journal of Manufacturing Science and Engineering's Best Paper Award in 2014, and the ASME Journal of Dynamic Systems, Measurement, and Control Best Paper Award in 2020. He is a Fellow of ASME, and a senior member of IEEE and SME.

Dr. Douglas Bristow is a Professor of Mechanical Engineering in the Department of Mechanical and Aerospace Engineering at the Missouri University of Science and Technology. He received his B.S. in Mechanical Engineering from Missouri S&T, Summa Cum Laude, in 2001. He received his M.S. and Ph.D., also in Mechanical Engineering, from the University of Illinois at Urbana-Champaign in 2003 and 2007, respectively. Dr. Bristow is the Director of the Center for Aerospace Manufacturing Technologies. His research interests include modeling, sensing and control development for precision motion problems, with particular interest in repetitive and layer-dynamic processes. Applications include additive manufacturing (powderbed fusion and direct energy deposition with powder metal, wire metal and wire glass) and metrology-in-theloop control of robotic machining and incremental sheet forming. In 2019 he received the ASME Rudolph Kalman Best Paper award.